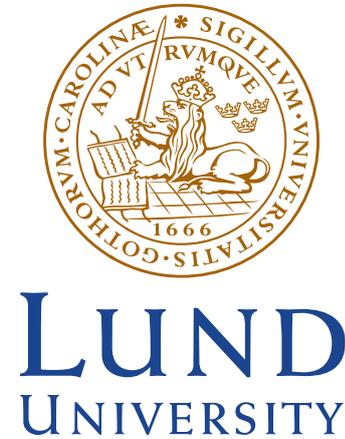# Towards More Efficient Wireless Power Transfer for 6G

Ali Al-Ameri and Jaeyoung Park
al1442al-s@stuent.lu.se, ja2132pa-s@stuent.lu.se

Department of Electrical and Information Technology
Lund University

Abstract

As time is moving forward, the world is becoming more dependent on Internet of Things (IoT) devices. The vision for the future involves IoT devices participating in various aspects of our daily lives, including sensing, controlling, and communicating. Such a future requires a significant number of IoT devices, which raises questions regarding sustainability in terms of battery waste. One promising candidate technology for providing power to IoT devices is Wireless Power Transfer (WPT). WPT can provide a convenient way of powering devices wirelessly, which decreases the need to use batteries.

It is known that the efficiency of a WPT system is highly dependent on the waveform used for power transmission, hence it is highly desirable to find waveform designs that enhance the end-to-end efficiency of WPT. In this work, our goal is to find waveforms that maximize the harvested power at the receiver of the WPT system, for a large number of transmitting antennas. We do this by developing a simulation framework using MATLAB, where we can do fast simulations for various system parameters, while taking into consideration the full characteristics of the WPT system.

Through our results we concluded that using Maximum Ratio Transmission is a viable waveform design strategy with low complexity. Using a larger number of antennas decreases the distortion caused by the amplifiers at the transmitter and increases the received power. Moreover, due to the receivers non-linearity, for a certain average power, having a waveform with a higher Peak to Average Power Ratio (PAPR) enhances the end-to-end WPT efficiency. However, this is only true up to a certain limit that depends on the rectifier circuit parameters. We also investigated several ways of deciding which subcarriers to use for transmission in the available bandwidth, and found a tone selection scheme aimed at maximizing the PAPR of the signal at the receiver while maintaining high efficiency at the transmitter with minimal distortion.

Popular Science Summary

Have you ever taken a moment to reflect on how wireless communication and the dawn of the information age have transformed our world? If someone from a century ago saw what we are able to do with devices in the palms of our hands, describing their astonishment as a mere "shock" would be an understatement. Now picture a future where we harness the same ability, but with energy transfer instead of information transfer. This is precisely the idea behind the topic of Wireless Power Transfer (WPT), where radio frequency signals are used to transfer power wirelessly through space, from an energy transmitter to an energy receiver. In principle, this would allow electricity to be sent through the air, much like how your Wi-Fi sends data.

Through WPT, we could have networks that conveniently power our ever increasing Internet of Things devices without batteries, even in environments that are inaccessible for humans, allowing for a significant reduction in battery waste and contributing to a more sustainable society.

There are numerous challenges that must be tackled to materialize WPT into a feasible and widely used reality. The biggest among these challenges is enhancing the efficiency of WPT. Higher efficiency leads to a larger WPT coverage area and the possibility of using WPT in a wider range of applications. This thesis recognizes the importance of enhancing the efficiency of WPT and focuses on this very challenge, by designing signals with characteristics that lead to increased WPT efficiency. We do this through computer simulations, by tweaking several signal parameters and assessing their impact on the harvested power at the energy receiver.

Through our investigations, we noted that finding the transmit signals that optimize the efficiency is a highly computationally demanding task, especially for systems with a large number of antennas. This is a major difficulty when designing signals for WPT. Therefore, in this thesis, to avoid the computational complexity concern, we explore using a heuristic signal design approach as a way of increasing the efficiency. As a result, we end up with simulations that demonstrate the effectiveness of using the heuristic approach, even when considering the entire WPT system characteristics with a large number of antennas. We also take a close look at the challenge associated with achieving efficient power transfer while minimizing interference with other systems. To get more details, we encourage you to read this thesis.

Acknowledgment

Table of Contents

List of Figures

Acronyms

AC Alternating Current.

BPF Bandpass Filter.

CSI Channel State Information.

DC Direct Current.

DL Downlink.

ER Energy Receiver.

ET Energy Transmitter.

FFT Fast Fourier Transform.

GD Gradient Descent.

IBO Input Back-Off.

IFFT Inverse Fast Fourier Transform.

IID Independent and Identically Distributed.

IoT Internet of Things.

LHS Left Hand Side.

LIS Large Intelligent Surfaces.

LOS Line-of-Sight.

LPF Lowpass Filter.

MIMO Multiple-Input Multiple-Output.

MPC Multi Path Component.

MRT Maximum Ratio Transmission.

OBO Output Back-Off.

OFDM Orthogonal Frequency Division Multiplexing.

OOB Out-of-band.

PA Power Amplifier.

PAPR Peak-to-Average Power Ratio.

RF Radio Freqeuncy.

RFID Radio Frequency Identification.

RHS Right Hand Side.

SCP Successive Convex Programming.

SCS Subcarrier Spacing.

SSPA Solid-State Power Amplifier.

TDD Time Division Duplex.

UL Uplink.

WEH Wireless Energy Harvesting.

WPT Wireless Power Transfer.

Introduction

1.1 Background and Motivation

In recent years, there has been a significant increase in research interest regarding the future of cellular communications, specifically focusing on the sixth generation of wireless systems, commonly known as 6G. This new phase has captured the attention of both academia and industry, who have set visions for the next generation of wireless systems. One such vision is to take steps towards enabling green connectivity through increased energy efficiency, especially by zero-energy/emission Internet of Things (IoT) deployments [1–4]. To achieve this, it is crucial to consider that one significant driver of emissions attributed to IoT devices is their reliance on compact batteries, which are primarily lithium-ion-based. Extensive studies on life cycle analysis have established that these batteries, during their production and disposal stages, contribute to environmental harm in terms of energy use and emissions [5, 6]. The use of these batteries is expected to experience a dramatic increase because as 5G continues to mature and 6G looms on the horizon, the number of IoT devices, serving various purposes such as sensing, controlling, and processing, is projected to experience a substantial increase [7]. This challenge becomes even more pronounced when considering that many IoT devices often require multiple battery replacements throughout their lifetimes since they outlast the batteries powering them. In fact the authors of [8] predict that 78 billion batteries powering IoT gadgets will be dumped everyday by 2025. Replacing batteries could also become a more challenging task in scenarios where IoT devices are deployed in hazardous environments, where it may be difficult or even impossible for humans to access.

Due to these environmental and practical issues associated with battery replacements in IoT devices, researchers have been looking into alternate strategies to power IoT devices and avoid the need for battery replacements. Energy harvesting techniques that harness energy from the surrounding environment, including light, thermal, wind, and vibration, offer a viable route in many applications due to their high efficiency combined with substantial energy density in terms of harvested power per unit area [9]. However, these energy collecting techniques heavily rely on the surrounding environment, posing potential limitations in various scenarios. Their effectiveness can be compromised by unpredictable conditions, and the availability of the ambient energy sources from the environment may be ob-

structed for extended durations. Furthermore, putting such methods into practice
requires additional hardware for energy harvesting, which can put practical re-
strictions on the form factor of IoT devices by making them bulkier. For these
reasons, in recent times, the research community have been looking at the poten-
tial of powering IoT devices using Radio Freqeuncy (RF) that might lead to a
breakthrough in overcoming the mentioned issues.

Powering devices using RF can be categorized into two different techniques,
namely Wireless Energy Harvesting (WEH) and Wireless Power Transfer (WPT)
[10]. Both of these technologies use RF to power a receiving device wirelessly.
Firstly, WEH is when the harvesting device or Energy Receiver (ER) collects RF
energy that is already available in the surrounding environment from, for example,
RF energy from existing base stations used solely for communication. In contrast,
WPT distinguishes itself from WEH, despite the fact that both technologies use
RF to provide power for devices. While WEH does not rely on a dedicated En-
ergy Transmitter (ET) and instead uses ambient RF energy from the environment,
WPT relies on transmitters designed specifically for energy transfer. This differ-
ence means that the transmitters in the case of WPT are controllable.

It is important to note that IoT devices typically receive much lower power
in the WEH case, compared to WPT, since WEH lacks control of the transmitter
for energy transfer optimization. Due to this, the majority of IoT devices cannot
work solely on WEH [10]. As a result, WPT is a more appealing choice compared
to WEH, since it provides more design flexibility and the possibility of achieving
significantly higher received power. WPT solves many of the mentioned issues as it
allows for powering of devices at a distance in a reliable manner. Having this ability
will reduce the need for replacing batteries which reduces battery waste. WPT can
also help to charge IoT devices in places that are inaccessible for humans. This is
particularly beneficial in scenarios where harvesting power from the environment
is not feasible, such as shadowed areas where traditional energy sources like solar
power may not be viable.

One thing to keep in mind is that WPT is mainly well-suited for low-power
devices such as IoT devices. Advancements in the semiconductor industry have
played a big role in making WPT a viable solution for providing power for such
IoT devices. The increased efficiency of integrated circuits resulting from these
advances has made computations less costly in terms of energy and allowed some
IoT devices to operate with low power consumption, as low as 10-100µW [3].
One good example of an existing application that uses WPT is Radio Frequency
Identification (RFID) [11]. In an RFID system, an RFID reader behaves as the
ET and sends an RF signal to communicate and power an RFID tag. The RFID
tag, which behaves as the ER, consists of a harvesting circuit and an integrated
circuit for processing, is powered up by the reader and then processes the received
information and then sends back a message to the reader. RFID tags do not use
any batteries and are entirely powered up by RF, which gives a glimpse of the
possibilities of WPT.

While WPT has many benefits, there are also challenges. The most important
challenge with WPT is low power transfer efficiency due to the wireless channel
in which the energy carrying transmitted electromagnetic waves propagate. This
sets limits on the distances that can be achieved with WPT in practice and it also

narrows down the possible applications where WPT can be a viable option. Other challenges include how to deal with exposure related safety risks and potential interference with other devices or systems. In order to overcome some of these challenges and make WPT more practical, many studies, such as [12], have focused on enhancing the overall efficiency, the so-called end-to-end efficiency, of power transfer from ET to ER. Most of the advances in WPT are mainly being done in two areas [10]. The first area, which is mainly being pursued by the electronics community, involves designing the characteristics of the receiver in a way that enhances the end-to-end efficiency [13]. The second area, which mainly relates to the wireless communication community, is focused on the design of transmit waveforms for WPT that increases the efficiency of power transfer and minimizes power loss due to propagation through the wireless channel [14–17]. The second area, despite the challenges of WPT, has the advantage of possibly using the rich existing literature of wireless communications, since a significant part of the advances in wireless communications can be applied for the benefit of WPT.

The above description motivates an investigation of waveform design approaches that enables efficient WPT. The goal is to maximize the harvested power at the ER by designing appropriate waveforms, considering the characteristics of both the transmitter and receiver. Of particular interest is to present a framework for finding waveform designs for efficient WPT in an environment with Large Intelligent Surfaces (LIS) and where Orthogonal Frequency Division Multiplexing (OFDM) is used. We focus on these, due to the fact that using a large number of antennas is a promising direction for new systems, and OFDM will most likely be used in the coming generations of wireless systems.

1.2   Problem Formulation and Limitations

Within the scope of this thesis, we focus on a single-user WPT system, in which the ET transmits energy to one ER. The authors of [14] explored transmit strategies aiming at maximizing the Direct Current (DC) output power harvested at the ER for an efficient single-user WPT system. The authors started their investigation under several assumptions, such as sufficiently weak incident RF signal at the input of the energy harvesting receiver, which allows them to model the WPT system. Based on this, they present a channel-adaptive waveform design scheme that maximizes the WPT performance. Furthermore, they expanded their work to account for an accurate characterization of the ER, and found waveforms that maximize the efficiency of WPT by solving an optimization problem. However, it is notable that the authors of [14] did not consider the characteristics and limitations of the transmitter.

By modeling the ET in a realistic manner, the authors of [18] proposed an optimized waveform solution when considering the end-to-end efficiency and demonstrated how the realistic characterization of the ET presented behaviour that could significantly degrade the energy harvesting efficiency of WPT. The authors of [18] successfully showed that this loss in efficiency could be reduced by their proposed waveform design optimization algorithm. Interestingly, the authors only showed their results for the single transmit antenna case. This algorithm will be revisited in this work where we take it a step further by analyzing it for the multiple transmit antenna case.

Our main objective is to formulate efficient waveform designs for systems featuring a large number of antennas, while accounting for the entirety of the WPT system characteristics. Our aim is to achieve this by using design strategies that maintain a low computational complexity, so that we can analyze waveform performance in such a system. By doing this, we intend to provide guidelines for heuristic waveform design approaches across various practical scenarios.

1.3   Methodology

In this thesis, we study different waveform design and power allocation strategies. In particular, we focus on investigating and designing waveforms for the goal of maximizing the harvested power at the ER. To achieve this goal, we use two approaches: an optimization approach using Successive Convex Programming (SCP) and a more practical, but sub-optimal, approach where we use Maximum Ratio Transmission (MRT). The limitations of the adopted optimization approach are discussed and a simulation framework for the MRT approach is presented. The presented simulation framework allows us to generate and analyze many results in MATLAB for different parameter setups, where we change: the channel model, the number of antennas at the transmitter, the number of subcarriers, the quality of the amplifier, and the subcarrier selections scheme.

1.4   Thesis Outline

This thesis is organized as follows: In Chapter 2, an overview of a WPT system is given followed by detailed discussions about efficiency and the various parts of a WPT system. In Chapter 3, the signal model used in this work is described, different waveform design approaches are discussed and the used simulation framework for generating the results is presented. In Chapter 4, the simulation results are shown and analyzed. Lastly, in Chapter 5 the conclusions of this thesis are drawn.

Technical Background

This chapter provides a general technical background on WPT systems. First, in Section 2.1, we discuss the structure of WPT systems. After that, in Section 2.2, we discuss the concept of end-to-end efficiency and how it can be broken down to three separate efficiencies. In Sections 2.3-2.5, we provide a description of each efficiency within the context of the corresponding components of the WPT system.

2.1 Overview of Wireless Power Transfer
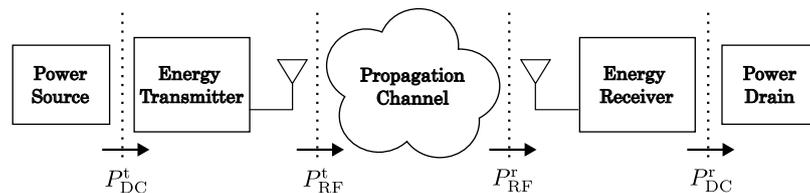
Figure 2.1: The block diagram of a generic wireless power transfer system, consisting of an ET and an ER, separated by a wireless channel, where $P_{\mathrm{DC}}^{\mathrm{t}}$ is the DC power at the transmitter, $P_{\mathrm{RF}}^{\mathrm{t}}$ the transmitted RF power, $P_{\mathrm{RF}}^{\mathrm{r}}$ the received RF power, and $P_{\mathrm{DC}}^{\mathrm{r}}$ the harvested DC power.

Figure 2.1 shows a generic WPT system consisting of an ET and an ER that are separated by a propagation channel. At the transmitter, the DC power $P_{\mathrm{DC}}^{\mathrm{t}}$ is used to generate the RF signal that propagates through the wireless channel, carrying the power $P_{\mathrm{RF}}^{\mathrm{t}}$. After passing through the channel, this RF signal arrives at the antenna of the ER with the power $P_{\mathrm{RF}}^{\mathrm{r}}$. Subsequent to its collection by the receiving antenna, the received RF signal then gets converted to a DC current with the power $P_{\mathrm{DC}}^{\mathrm{r}}$ which can then be used to power a device. We want to make this harvested power, $P_{\mathrm{DC}}^{\mathrm{r}}$, as large as possible by maximizing the efficiency of the system.

During power transfer, the waveform of the transmitted signal plays a crucial role in determining the efficiency of the system. As highlighted in the introduction, this work aims to maximize the power harvested at the receiver. Studies, such as [19], have demonstrated that using a multi-sine based signal, offering high

Peak-to-Average Power Ratio (PAPR), maximizes the power harvested by the receiver, by allowing the receiver to operate at a higher efficiency. Therefore, this thesis exclusively focuses on waveforms based on multi-sine signals. Among these, multi-sine transmissions such as OFDM have been considered. OFDM, with its capability to reach a high PAPR, is already used in cellular systems and is expected to be used in the next generation of wireless systems. This means that it is particularly interesting to investigate OFDM for possible integration of cellular communications with WPT.

2.2 End-to-End Efficiency of a WPT System

In order to design an efficient WPT system, the first step is to describe and quantify what is meant by efficiency. The end-to-end efficiency of the entire system is described as

$$e = \frac{P_{\mathrm{DC}}^{\mathrm{r}}}{P_{\mathrm{DC}}^{\mathrm{t}}}. \tag{2.1}$$

Since the WPT system consists of an ET, a channel and an ER, the end-to-end efficiency can be factored into a product of three distinct efficiencies as

$$e = \frac{P_{\mathrm{DC}}^{\mathrm{r}}}{P_{\mathrm{DC}}^{\mathrm{t}}} = e_1 \cdot e_2 \cdot e_3, \tag{2.2}$$

where e_1 is the DC-RF efficiency, e_2 is the RF-RF efficiency and e_3 is the RF-DC efficiency.

Initially, one may assume that independent maximization of the three efficiencies stated in (2.2) would suffice to improve the overall end-to-end efficiency. However, due to the non-linear characteristics of the transmitter and receiver, all three efficiencies must be considered simultaneously. This crucial aspect becomes evident as we venture into more in-depth explanations of these efficiencies in the following sections. In particular, it will become evident that, as a result of the non-linear behaviours, waveform properties that improve one of the three efficiencies may reduce the other two. To understand the intricate connections between the different efficiencies, let us first start by looking at the ET in the next section.

2.3 Energy Transmitter and DC-RF Efficiency
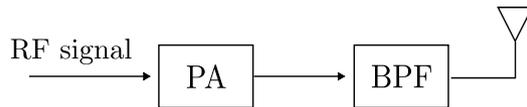
Figure 2.2: The structure of an ET consisting of a single RF chain with a single antenna, the PA block is the power amplifier and the BPF block is the bandpass filter.

The ET is responsible for generating and transmitting signals through the wireless channel. At the ET, a DC power source is used to generate the baseband signals, which are then upconverted to RF. After that, depending on whether a single or multiple antenna transmitter is employed, the generated RF signal will pass through either a single or multiple RF chains. Figure 2.2 shows a basic structure of an ET with a single RF chain, consisting of a Power Amplifier (PA), Bandpass Filter (BPF) and a transmitting antenna. The RF signal at the input of the RF chain is firstly amplified by a PA, filtered through a BPF, and finally fed into the transmitting antenna.

2.3.1 DC-RF Conversion Efficiency
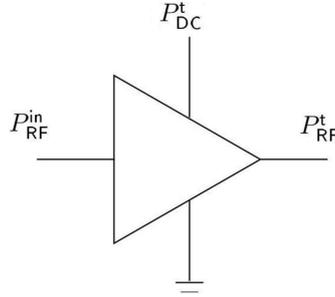
Figure 2.3: A power amplifier schematic with power notations.

Determining the DC-RF efficiency, can be done by evaluating the relationship between the transmitter's output power level and its input power. Assuming that everything in the transmitter shown in Figure 2.2 operates in a lossless manner except for the PA, then one can find e_1 by calculating the efficiency of the PA.

Figure 2.3 shows the basic structure of a PA, where $P_{\mathrm{RF}}^{\mathrm{t}}$ is the output power from the input power $P_{\mathrm{RF}}^{\mathrm{in}}$ and the DC power supply $P_{\mathrm{DC}}^{\mathrm{t}}$. From these quantities, e_1 can be found as

$$e_1 = \frac{P_{\mathrm{RF}}^{\mathrm{t}}}{P_{\mathrm{DC}}^{\mathrm{t}}}. \tag{2.3}$$

Incorporating the effect of the input RF signal, the efficiency, referred to as power-added efficiency, is expressed as

$$e_{\mathrm{Power-Added}} = \frac{P_{\mathrm{RF}}^{\mathrm{t}} - P_{\mathrm{RF}}^{\mathrm{in}}}{P_{\mathrm{DC}}^{\mathrm{t}}}. \tag{2.4}$$

In this thesis, the measure in (2.3) is used for the DC to RF conversion efficiency.

2.3.2 PA and Non-linear Behaviour

The PA is an active electronic device that takes an input signal and outputs it with a higher power. Ideally, the output signal should be identical to the input signal except that it has a higher power. However, PAs are unable to do that since they are non-linear devices. This non-linear behaviour depends on several factors

such as device characteristics, operating conditions, and input signal amplitude. Non-linearity in power amplifiers generates undesirable harmonics and other types of distortion which alter the input signal waveform. This distortion degrades the efficiency of the amplifier and leads to potential interference with adjacent frequency bands. In this thesis, the amplifier and its non-linearity is modeled as a Solid-State Power Amplifier (SSPA) using the Rapp model [20],

$$x^{\text{out}}(t) = \frac{Gx^{\text{in}}(t)}{\left[1 + \left(\frac{G|x^{\text{in}}(t)|}{A_s}\right)^{2\beta}\right]^{\frac{1}{2\beta}}}, \tag{2.5}$$

where $x^{\text{out}}(t)$ is the output signal and $x^{\text{in}}(t)$ is input signal. This model uses three key parameters to effectively capture the distortion caused by the amplifier and represent its saturation behaviour. Firstly, the parameter G represents the small-signal amplifier gain. The parameter A_{s} represents the saturation voltage of the amplifier and lastly, β is the smoothing factor which controls the smoothness of the transition between the linear region and the saturated region.

Figure 2.4 depicts the characteristics of the PA as described above. It can be noted that the gain of the PA is related to the slope of its response inside the linear region. Additionally, the maximum power that the amplifier can output is $P_{\text{sat}}^{\text{out}} = \frac{A_{\text{s}}^2}{2}$, which is achieved at the input power $P_{\text{sat}}^{\text{in}}$. For the black solid curve, β is infinite since the transition from linear to non-linear region is instantaneous. The figure also demonstrates the decline in the transmitter efficiency caused by the non-linear characteristics of the PA. It becomes noticeable that beyond a certain threshold, increasing the input power does not translate to a proportional increase in the output power due to the saturation of the amplifier.

Figure 2.4 also highlights one common method that is used to mitigate the non-linear behaviour of an amplifier, i.e., by having a "back-off" to ensure that the amplifier operates in the linear region. This is done by first deciding an operation point, which is a point in the response graph where the desired behaviour of the amplifier is attained, and after that intentionally limiting the power of the amplifier so that this operation point is achieved. In general, backing-off can be done either through Output Back-Off (OBO) or Input Back-Off (IBO), where OBO puts a normalization factor on the output power of the amplifier, while IBO is done through normalization of the input. These concepts are useful for our case since we want to reduce the distortion of the PAs and maximize the DC-RF efficiency. However, it should be noted that in the end it is the amplitude of the signal that determines how much it will be distorted due to the non-linear behaviour of the PA. This is why the efficiency of the ET can still suffer when transmitting a high PAPR OFDM signal, even if the signal has a low average power.

2.4   Propagation Channel and RF-RF Efficiency

WPT systems heavily depend on the propagation channel properties to transmit RF signal from the ET to the ER. A comprehensive understanding of propagation channel effects is crucial for the design and optimization of WPT systems.
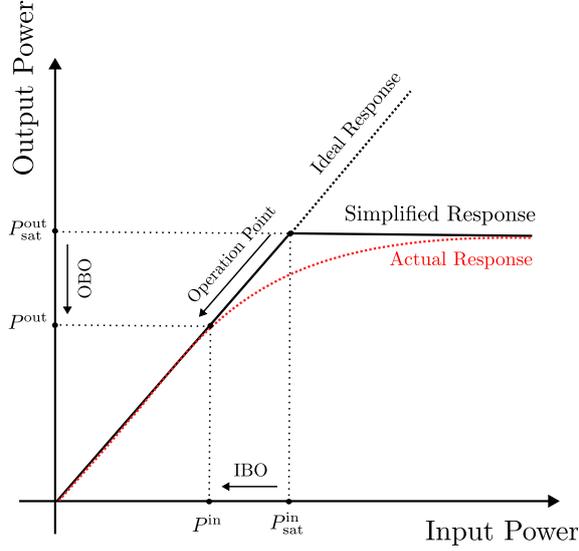
Figure 2.4: Comparing the characteristics of simplified PA (solid black curve) with a realistic PA (dotted red curve). The concept of IBO and OBO is illustrated.

Characteristics such as path loss, small-scale fading, shadowing, and multi-path propagation have significant influence on the design of transmit waveforms for maximum received power at the ER.

2.4.1 RF-RF Conversion Efficiency

The second efficiency of the WPT system, e_2, is the RF-RF efficiency which indicates the effectiveness of conversion of RF power at the transmitter into RF power at the receiver, after passing through the propagation channel, as

$$e_2 = \frac{P_{RF}^r}{P_{RF}^t}. \tag{2.6}$$

The RF-RF efficiency is typically the lowest efficiency of the three included in (2.2). The reason for this is mainly due to path-loss, since the signal experiences significant attenuation as it propagates over the distance between the ET and ER. Several strategies could mitigate this to a certain degree, such as leveraging antennas with high directivity or, as will be seen in the following subsection, using large arrays combined with beamforming strategies.

2.4.2 Array Gain

Combating path-loss in order to increase the efficiency of the WPT system can be done through intelligent use of the signal propagation environment by techniques such as adaptive energy beamforming. This technique enhances the RF-RF efficiency in WPT by directing transmission signals to a specific direction, by

adjusting the phase and amplitude of the signals. Directing the signals in this manner can increase the power at the receiving antenna by the array gain. As the name implies, to achieve this gain, the transmitter has be in the form of an array which means that it has to be equipped with multiple antennas. This array gain is proportional to the size of the array in terms of number of antenna elements. For this reason, the use of an ET with a massive number of antennas such as in massive Multiple-Input Multiple-Output (MIMO) or its extension, LIS, is of huge interest for WPT applications. LIS is an emerging technology envisioned to be used in 6G communications with huge arrays comprising hundreds of antennas or more [21–23].

2.4.3   Channel Knowledge

To achieve the advantages offered by large arrays as mentioned in the preceding subsection and effectively beam-form the transmission towards the ER, the availability of Channel State Information (CSI) becomes essential. CSI can be acquired using techniques similar to those developed in wireless communication systems, such as those based on reciprocity. In those techniques, the Uplink (UL) channel is estimated through pilot transmissions by the receiver and based on the UL estimate, the Downlink (DL) channel knowledge is acquired since the radio channel is the same in the UL and DL [24,25]. There are other channel acquisition techniques from wireless communications based on feedback [14].

However, since these techniques are developed for wireless communications, they do not take into account some of the characteristics of WPT. First, while receivers in wireless communications need CSI for coherent detection of the received signals, receivers in WPT do not need CSI, since they convert the received RF signal directly to a DC current. Second, when designing CSI acquisition schemes for WPT, it is important to take into account the restricted hardware processing capability of receiving devices. For example, IoT devices in wireless sensing applications may lack the sophisticated channel estimation or signal processing abilities of conventional wireless communication systems. Last, it is crucial to consider how the designed channel acquisition scheme affects the net harvested energy by examining the trade off between the gain achieved by using the designed scheme when transmitting versus the power consumed by the ER for the purpose of CSI acquisition. Addressing these challenges when designing CSI acquisition schemes for WPT is an area of ongoing research where developments are being made such as the power probing concept proposed in [26,27] where, to save energy at the ER, the ER transmits very limited feedback for channel acquisition.

2.5 Energy Receiver and RF-DC Efficiency
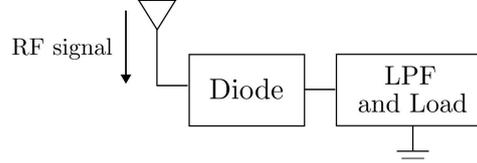
Figure 2.5: Block diagram of an ER with a single antenna, featuring a rectifier that consists of a diode, LPF, and load.

Figure 2.5 shows the third component of the WPT system, which is the ER. The ER consists of an antenna and a rectifier, commonly known as a rectenna. The rectifier uses one or more diodes, a Lowpass Filter (LPF), and a load in its operation. The main purpose of the ER is to collect the RF energy emitted by the ET. The ER does this through reception of the RF signal by the receiver antenna, followed by conversion of the received signal into a DC current by the rectifier. Finally, this DC current is used at the load. Figure 2.6 provides a visual representation of the equivalent circuit of the antenna and the rectifier when a single antenna is used. In this work, we use this simple single diode model to make the analysis tractable. However, there are other more advanced rectifier models that use several diodes [13].
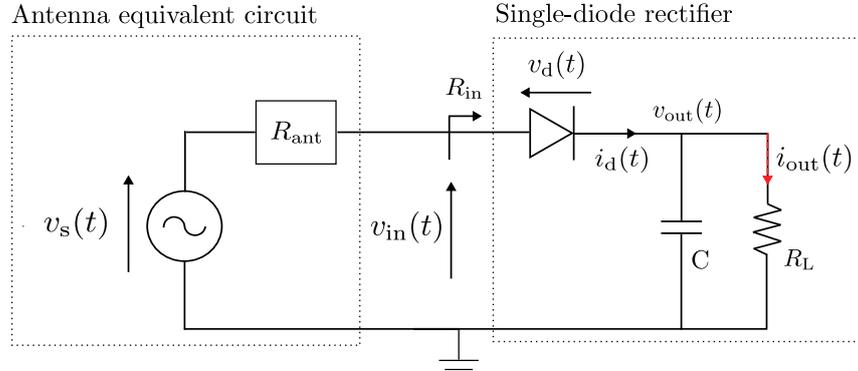
Figure 2.6: Circuit model of a single diode rectifier with a single antenna, low-pass filter, and load resistance.

2.5.1 RF-DC Conversion Efficiency

The third efficiency in a WPT system, the RF-DC conversion efficiency, e_3, is written as

$$e_3 = \frac{P_{\mathrm{DC}}^{\mathrm{r}}}{P_{\mathrm{RF}}^{\mathrm{r}}}, \tag{2.7}$$

and it refers to the receiver's ability to convert RF power at its input into DC power at its output. Assuming that the entire ER is lossless, except for the rectifier, then

e_3 is equivalent to the efficiency of the rectifier.

2.5.2   Antenna Model

The first component in the ER is the receiving antenna which operates as the interface between the wireless channel and the receiver. As shown in Figure 2.6, we model the receiving antenna as a voltage source $v_{\mathrm{s}}(t)$ followed by a series resistance R_{ant}. An antenna receives electromagnetic energy from the wireless channel, then the energy captured by the antenna is transferred from the antenna to the rectifier through the matching network. The input impedance of the rectifier is denoted by

$$Z_{\mathrm{in}} = R_{\mathrm{in}} + jX_{\mathrm{in}} \tag{2.8}$$

where R_{in} and X_{in} are the input resistance and reactance of the rectifier, respectively. Assuming perfect matching, Z_{in} can be written as $Z_{\mathrm{in}} = R_{\mathrm{in}} = R_{\mathrm{ant}}$, where $X_{\mathrm{in}} = 0$. Then, the input voltage to the rectifier can be expressed as

$$v_{\mathrm{in}}(t) = v_{\mathrm{s}}(t)/2 \,. \tag{2.9}$$

We define the power received by the antenna as

$$P_{\mathrm{rf}}^{\mathrm{r}} = \varepsilon\{y(t)^2\}, \tag{2.10}$$

where $y(t)$ denotes the RF signal impinging on the receiver antenna, and $\varepsilon\{\cdot\}$ denotes the expectation operator over time, which is the same as integrating over the period. Based on [15], we assume that all of this received RF power is transferred to the rectifier. Therefore, by using simple circuit theory, the received power is also expressed as $P_{\mathrm{rf}}^{\mathrm{r}} = \varepsilon\{v_{\mathrm{in}}(t)^2\}/R_{\mathrm{in}}$, and the rectifier input voltage becomes

$$v_{\mathrm{in}}(t) = y(t)\sqrt{R_{\mathrm{in}}} = y(t)\sqrt{R_{\mathrm{ant}}}. \tag{2.11}$$

2.5.3   Rectifier and Non-linear Behaviour

The rectifier is an essential component in the ER. The purpose of the rectifier is to convert the alternating current provided by the antenna into DC current. Typically, diodes are used in rectifiers which cause the non-linear behaviour of the ER. In general, the diode is described by its non-linear I-V characteristics shown in Figure 2.7. The I-V characteristics can be divided into three regions, the forward bias region, the off state region, and the breakdown region. The region the diode operates in depends on the voltage drop across the diode $v_{\mathrm{d}}(t)$. For a diode with reverse breakdown voltage v_{br} and turn on voltage v_{T}, it can be seen that when $v_{\mathrm{d}}(t) > v_{\mathrm{T}}$, the diode operates in the forward bias region which means that a current $i_{\mathrm{d}}(t)$ starts flowing through the diode in the forward direction, resulting in power being harvested. When $-v_{\mathrm{br}} < v_{\mathrm{d}}(t) < v_{\mathrm{T}}$, the diode is in the off state region, which, as the name suggests, means that the diode does not conduct any significant current. Finally, when $v_{\mathrm{d}}(t) < -v_{\mathrm{br}}$, the diode operates in the breakdown region, conducting current in the reverse direction.
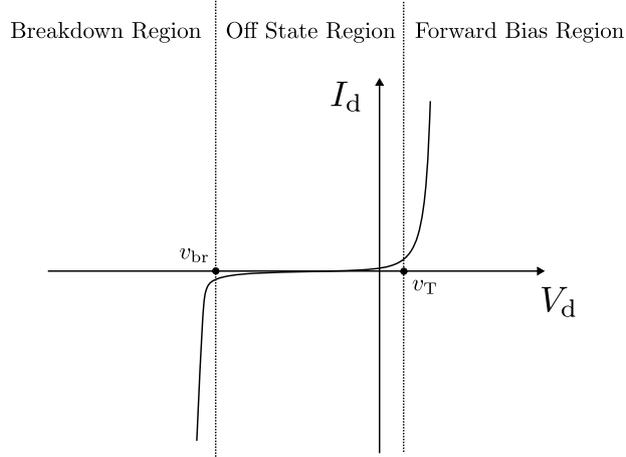
Figure 2.7: Schematic of the diode I-V curve illustrating breakdown and turn-on voltages. The figure also depicts the three operational regions for a diode.

The behaviour of the diode can also be observed mathematically by analyzing the diode characteristic equation expressed in [17], as

$$i_{\mathrm{d}}(t) = i_{\mathrm{s}}\left(e^{\frac{v_{\mathrm{d}}(t)}{\eta v_{\mathrm{t}}}} - 1\right) - i_{\mathrm{bv}}\left(e^{\frac{-(v_{\mathrm{d}}(t)+v_{\mathrm{br}})}{\eta v_{\mathrm{t}}}}\right), \qquad (2.12)$$

where i_{s} denotes the reverse bias saturation current, v_{t} the thermal voltage with a typical value of 25 mV, η the ideality factor of the diode, and i_{bv} the the diode breakdown saturation current. The first exponential term governs the behaviour of the diode when it is in the forward bias region, while the second exponential term determines the behaviour of the diode in the breakdown region. When the diode is in the turnoff region then both of these exponential terms are close to zero and the current flowing through the diode becomes negligible. From this equation, one can conclude that as the diode voltage $v_{\mathrm{d}}(t)$ grows, the current flowing through the diode increases exponentially resulting in an increase in the harvested power $P_{\mathrm{DC}}^{\mathrm{r}}$. This growth continues until the amplitude of $v_{\mathrm{d}}(t)$ starts approaching the reverse breakdown voltage, at which a sudden increase of the current flowing in the opposite direction occurs. When this happens, the net current flows in the forward direction, and the harvested power $P_{\mathrm{DC}}^{\mathrm{r}}$ saturates, since the two exponential terms in (2.12) will grow at the same rate but with opposite signs, resulting in them taking each other out. Figure 2.8 demonstrates the effect of this behaviour on the harvested DC power and conversion efficiency schematically. Since the diode voltage and the received RF power are proportional, the schematic behaves exactly as described by the general diode characteristic equation. An increase in the received power increases the harvested power until the received power becomes so large that the diode voltage reaches breakdown, then the harvested power saturates and the RF-DC efficiency starts to degrade.

Now that we have described the diode characteristics, let us move on to model
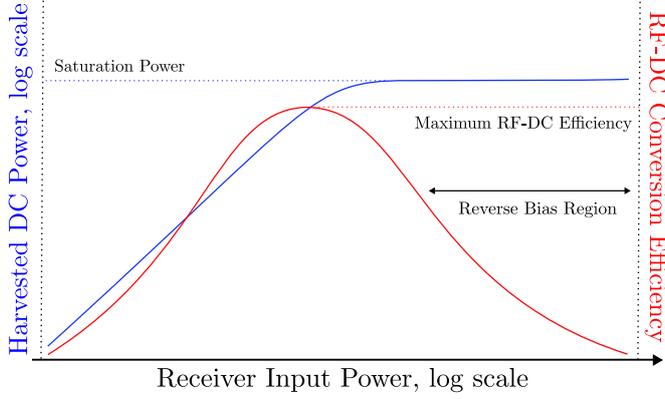
Figure 2.8: Schematic of the of harvested DC power. The blue curve represents the harvested DC power $P_{\mathrm{DC}}^{\mathrm{r}}$ vs received input power $P_{\mathrm{RF}}^{\mathrm{r}}$. The red curve represents the RF-DC efficiency over the received input power.

the receiver by analyzing the receiver circuit shown in Figure 2.6. The main interest is to express the output current, $i_{\mathrm{out}}(t)$, going through the load R_{L}, as a function of the received signal at the input of the receiver $y(t)$. To do this, we adopt the approach introduced by [17], and follow their derivations, where in order to capture the complete behaviour of the diode, they use the model in (2.12). Through simple algebraic manipulations using nodal analysis on the receiver circuit, the relationship between input voltage and output current is obtained as

$$
\begin{aligned}
i_{\mathrm{s}} &\left(e^{\frac{v_{\mathrm{in}}(t)-i_{\mathrm{out}}(t)R_{\mathrm{L}}}{\eta v_{\mathrm{t}}}} - 1 \right) - i_{bv} \left(e^{\frac{-(v_{\mathrm{in}}(t)-i_{\mathrm{out}}R_{\mathrm{L}}+v_{\mathrm{br}})}{\eta v_{\mathrm{t}}}} \right) \\
&= R_{\mathrm{L}}C\frac{di_{\mathrm{out}}(t)}{dt} + i_{\mathrm{out}}(t).
\end{aligned}
\tag{2.13}
$$

Based on [17], the input voltage, $v_{\mathrm{in}}(t)$, is assumed to be a periodic Alternating Current (AC) signal, the output current, $i_{\mathrm{out}}(t)$, is also periodic with the same periodicity, which we denote with T. To separate between the periodic and constant parts of the output signal, we express it as $i_{\mathrm{out}}(t) = \bar{i}_{\mathrm{out}} + \tilde{i}_{\mathrm{out}}(t)$, where $\bar{i}_{\mathrm{out}}$ and $\tilde{i}_{\mathrm{out}}(t)$ denote the DC and AC components of the output current, respectively. By averaging the Left Hand Side (LHS) and Right Hand Side (RHS) of (2.13) over T, we get

$$
\begin{aligned}
i_{\mathrm{s}} &\left(\frac{1}{T} e^{-\frac{\bar{i}_{\mathrm{out}}R_{\mathrm{L}}}{\eta v_{\mathrm{t}}}} \int_{T} e^{\frac{v_{\mathrm{in}}(t)-\tilde{i}_{\mathrm{out}}(t)R_{\mathrm{L}}}{\eta v_{\mathrm{t}}}} dt - 1 \right) \\
&- i_{\mathrm{bv}} \left(\frac{1}{T} e^{\frac{\bar{i}_{\mathrm{out}}R_{\mathrm{L}}-v_{\mathrm{br}}}{\eta v_{\mathrm{t}}}} \int_{T} e^{\frac{-v_{\mathrm{in}}(t)+\tilde{i}_{\mathrm{out}}(t)R_{\mathrm{L}}}{\eta v_{\mathrm{t}}}} dt \right) \\
&= \frac{R_{\mathrm{L}}C}{T} \int_{T} \frac{d\tilde{i}_{\mathrm{out}}(t)}{dt} dt + \frac{1}{T} \int_{T} (\bar{i}_{\mathrm{out}} + \tilde{i}_{\mathrm{out}}(t)) dt \\
&= \bar{i}_{\mathrm{out}}.
\end{aligned}
\tag{2.14}
$$

Like in [17], we assume that the capacitance of the LPF is large, i.e., $C >> \frac{T}{R_L}$. As a consequence, the AC component of the output current is small and can be neglected. This simplifies (2.14) to

$$
\begin{aligned}
&i_s \left(\frac{1}{T} e^{-\frac{\bar{i}_{out} R_L}{\eta v_t}} \int_T e^{\frac{v_{in}(t)}{\eta v_t}} dt - 1 \right) \\
&- i_{bv} \left(\frac{1}{T} e^{\frac{\bar{i}_{out} R_L - v_{br}}{\eta v_t}} \int_T e^{\frac{-v_{in}(t)}{\eta v_t}} dt \right) \\
&= \bar{i}_{out}.
\end{aligned}
\tag{2.15}
$$

By using the symmetry $\frac{1}{T} \int_T e^{\frac{v_{in}(t)}{\eta v_t}} dt = \frac{1}{T} \int_T e^{-\frac{v_{in}(t)}{\eta v_t}} dt$, which holds since $v_{in}(t)$ is assumed to be periodic, and by replacing $v_{in}(t)$ using (2.11), (2.15) can be written as

$$
\frac{e^{\frac{\bar{i}_{out} R_L}{\eta v_t}} \left(1 + \frac{\bar{i}_{out}}{i_s} \right)}{1 - \left(\frac{i_{bv}}{i_s} \right) e^{\frac{2\bar{i}_{out} R_L - v_{br}}{\eta v_t}}} = \frac{1}{T} \int_T e^{\frac{\sqrt{R_{ant}} y(t)}{\eta v_t}} dt,
\tag{2.16}
$$

where only the LHS has a dependency on $\bar{i}_{out}$. In (2.16), the RHS is non-negative which means that

$$
\bar{i}_{out} < \frac{1}{2R_L} \left(\eta v_t ln(\frac{i_s}{i_{bv}}) + v_{br} \right).
$$

Since (2.16) is based on (2.12), it can be noted that the relationship between rectenna output DC current and the incident RF signal is fully captured. However, there is an alternative approach for modeling the ER. This approach was first introduced by [14, 15] where for simplicity, the diode model used only considers the off state and forward bias regions as

$$
i_d(t) = i_s \left(e^{\frac{v_d(t)}{\eta v_t}} - 1 \right).
\tag{2.17}
$$

This simplification can be made as long as the peak RF power at the input of the receiver is sufficiently low, such that the diode operates far enough from the breakdown region. Following [14, 15], by Taylor expansion of the simplified diode characteristic in (2.17), around an operating point $v_d = a$, a tractable diode model is obtained as

$$
\begin{aligned}
i_d(t) &= i_s(e^{\frac{v_d(t)}{\eta v_t}} - 1) = \sum_{i=0}^{\infty} k_i'(v_d(t) - a)^i, \\
\text{where } k_i' &= \begin{cases} i_s(e^{\frac{a}{\eta v_t}} - 1), & \text{if } i = 0 \\ i_s \dfrac{e^{\frac{a}{\eta v_t}}}{i!(\eta v_t)^i}, & \text{if } i = 1, ..., \infty. \end{cases}
\end{aligned}
\tag{2.18}
$$

The current going through the diode, $i_d(t)$, is directed through an LPF, as depicted in Figure 2.6, to remove the high-frequency signal components and output a DC current. By assuming a steady-state response, employing an ideal LPF (which allows us to drop the time dependency in $v_{out}(t)$ and $i_{out}(t)$), and selecting $a = \varepsilon\{v_d(t)\} = -v_{out}$, (2.18) can be expressed as

$$i_{\mathrm{d}}(t) = k_0' + \sum_{i=1}^{\infty} k_i'(v_{\mathrm{d}}(t) - v_{\mathrm{out}})^i = k_0' + \sum_{i=1}^{\infty} k_i' v_{\mathrm{in}}(t)^i. \tag{2.19}$$

Replacing $v_{\mathrm{in}}(t)$ with (2.11), (2.19) becomes

$$i_{\mathrm{d}}(t) = k_0' + \sum_{i=1}^{\infty} k_i' R_{\mathrm{ant}}^{i/2} y(t)^i. \tag{2.20}$$

The output current going through the load i_{out} is found by taking the DC component of $i_{\mathrm{d}}(t)$ which is the time average of the current going through the diode, and is written as

$$i_{\mathrm{out}} = \varepsilon\{i_{\mathrm{d}}(t)\} = k_0' + \sum_{i \geqslant 2,\,\mathrm{even}}^{n_0} k_i' R_{\mathrm{ant}}^{i/2} \varepsilon\{y(t)^i\}, \tag{2.21}$$

where we have truncated the series to n_0 terms where n_0 is a positive even integer since $\varepsilon\{y(t)^i\} = 0$ for all odd values of i. Since k_i' are functions of $a = -v_{\mathrm{out}} = -R_{\mathrm{L}} i_{\mathrm{out}}$, we use an approximation of the output current as

$$z_{\mathrm{DC}} = \sum_{i \geqslant 2,\,\mathrm{even}}^{n_0} k_i R_{\mathrm{ant}}^{i/2} \varepsilon\{y(t)^i\},$$
$$\text{where } k_i = \frac{i_{\mathrm{s}}}{i!(n_{\mathrm{f}} v_{\mathrm{t}})^i}. \tag{2.22}$$

Now, we have an explicit current measure z_{DC} that is expressed with diode characteristics k_i that are independent of the operating point a. Note that the approximation z_{DC} is particularly useful for optimization, since a waveform that optimizes it also maximizes i_{out}. Finally, $n_0 = 4$ is chosen so that (2.22) becomes

$$z_{\mathrm{DC}} = k_2 R_{\mathrm{ant}} \varepsilon\{y(t)^2\} + k_4 R_{\mathrm{ant}}^2 \varepsilon\{y(t)^4\}, \tag{2.23}$$

which represent the linearity of the diode current with the first term, while the non-linearity is characterized with the second term.

Now, let us move on to discuss how to maximizes the RF-DC efficiency. From Figure 2.6, it can be seen that to maximize this efficiency, the average current going through the diode has to be as large as possible. As we saw in the analysis of the diode, the average current going through the diode increases exponentially with the amplitude of the diode voltage $v_{\mathrm{d}}(t)$, until the breakdown region. This means that if we stay within the forward bias region, for a given average signal power, higher amplitude signals $y(t)$ will lead to better RF-DC efficiency. However, there is a restriction to this. Assuming that the received signal is a multi-sine signal that can be expressed as a superposition of N sinusoids, with a pulse length δ, and a period T, then it seems necessary to establish a bound on the PAPR of this signal as

$$\mathrm{PAPR} < \frac{\delta_{\mathrm{opt}}}{T} = \frac{R_{\mathrm{L}} - R_{\mathrm{ant}}}{R_{\mathrm{ant}}}, \tag{2.24}$$

where δ_{opt} is the optimal pulse length. If the PAPR of the received signal is higher than this bound, then the harvester efficiency experiences a dramatic drop. We
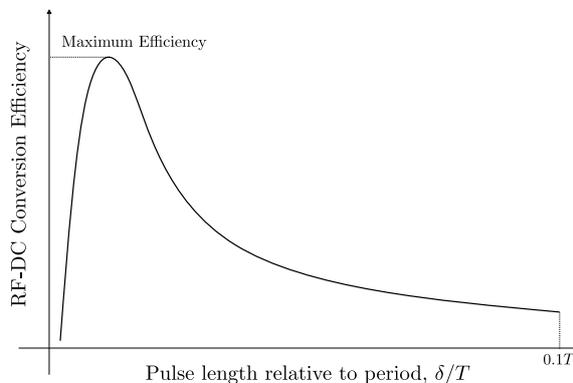
Figure 2.9: RF-DC efficiency as a function of the relative pulse length δ/T.

present the above bound without any proof, as it goes beyond the scope of this work. However, we demonstrate the bound in (2.24) with Figure 2.9. We move through this figure from right to left by increasing the number of tones, since for our multi-sine signal, a bigger N will lead to a smaller δ. Now, by keeping the period and average power of the signal unchanged, this shorter δ leads to a higher PAPR which leads to a higher current going through the diode. At some point, current flowing through the diode reaches a magnitude where the power dissipated across the antenna resistance becomes considerable. This leads to a significant drop in the harvester efficiency, which is reflected in the figure, since as we continue traversing from right to left, we eventually move past the point of maximum efficiency, which is achieved when $\delta = \delta_{\mathrm{opt}}$. To avoid reaching this efficiency drop, the number of tones has to be chosen in a way that keeps the PAPR within the bound in (2.24).

From the above explanation, the difficulty of finding waveforms that maximize the scaled output DC current emerges. The non-linearities of the transmitter and receiver create the difficulty where a waveform that maximizes the DC-RF efficiency, contradicts what a good waveform should be for maximizing the RF-DC efficiency.

It can be noted that we have chosen to use two ways of representing the relationship between the received signal and output DC current. As mentioned, the relation presented in (2.23) is based on the assumption that the diode at the rectifier is operating far from its breakdown region. In most WPT scenarios, this assumption holds true due to path-loss, resulting in relatively low peak received RF power. However, as discussed in Subsection 2.4.2, using large arrays can vastly improve RF-RF efficiency, leading to high peak RF power at the receivers input. In such cases, the diode can reach its breakdown region, necessitating the use of the more accurate relation in (2.16) that takes into consideration the full diode behaviour. In the following chapters, we will adopt (2.23) for designing optimal waveforms in systems with a limited number of antennas and subcarriers, while for larger systems, where the potential for diode breakdown exists, we use (2.16).

Signal Model and Waveform Design

This chapter primarily focuses on the signal model used in this work and various waveform design strategies. Chapter 3.1 provides a comprehensive overview of the signal model. In Chapter 3.2, we discuss the optimization based approach to waveform design and the challenges associated with this approach. Finally, in Chapter 3.3, we introduce an alternative waveform design approach and its corresponding simulation framework.

3.1 Signal Model for Multiple Antenna Transmitter
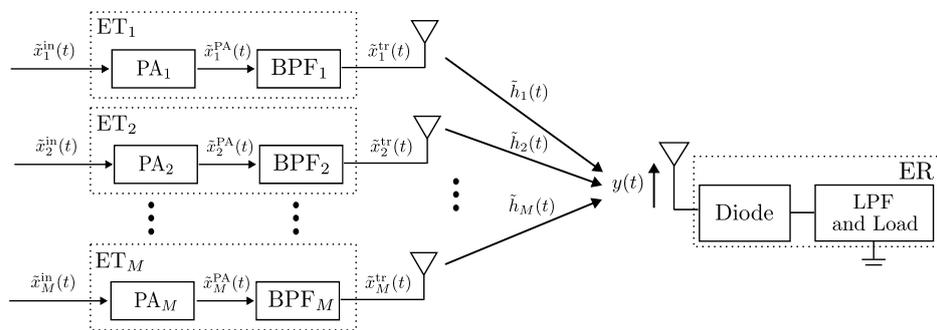
Figure 3.1: The WPT structure with non-linear PAs and rectenna.

As described earlier, we focus, in this thesis, on waveform design for a single user WPT system where the ET consists of a massive number of antennas. Figure 3.1 illustrates a block diagram of such a system, used in [18], consisting of an M-antenna ET, and a single-antenna ER. In this figure, $\tilde{x}_m^{\text{in}}(t)$ and $\tilde{x}_m^{\text{PA}}(t)$ represent signals at the input and output of the m-th PA respectively. $\tilde{x}_m^{\text{tr}}(t)$ is the complex transmit signal, which is at the output of the m-th BPF and $\tilde{h}_m(t)$ the time domain impulse response representing the channel from the m-th transmit antenna to the ER. Finally, $y(t)$ is the received signal at the ER. As previously mentioned, we assume that transmission in the ET is based on OFDM. Let us assume that each OFDM transmission consists of N different subcarriers in the frequency band $[f_{\text{min}}, f_{\text{max}}]$ with bandwidth $B = f_{\text{max}} - f_{\text{min}}$ in hertz (Hz).

21

Assuming $\widetilde{W}_{n,m}^{\text{in}}$ is the input complex weight of the n-th subcarrier at the m-th antenna, and f_n is the frequency of the n-th subcarrier, the complex input signal, $\tilde{x}_m^{\text{in}}(t)$, can then be expressed as

$$\tilde{x}_m^{\text{in}}(t) = \sum_{n=0}^{N-1} \sqrt{2}\widetilde{W}_{n,m}^{\text{in}} e^{j2\pi f_n t}. \tag{3.1}$$

This signal is then amplified through the PA. Using the Rapp model from (2.5), the amplified complex signals, $\tilde{x}_m^{\text{PA}}(t)$, is given by

$$\tilde{x}_m^{\text{PA}}(t) = f_{\text{SSPA}}(\tilde{x}_m^{\text{in}}(t)) = \frac{G\tilde{x}_m^{\text{in}}(t)}{\left[1 + \left(\frac{G|\tilde{x}_m^{\text{in}}(t)|}{A_s}\right)^{2\beta}\right]^{\frac{1}{2\beta}}}. \tag{3.2}$$

The signal $\tilde{x}_m^{\text{PA}}(t)$ then passes through an ideal BPF before its transmission. The complex transmit signal on the m-th antenna is written as

$$\tilde{x}_m^{\text{tr}}(t) = \sum_{n=0}^{N-1} \sqrt{2}\widetilde{W}_{n,m}^{\text{tr}} e^{j2\pi f_n t}, \tag{3.3}$$

where $\widetilde{W}_{n,m}^{\text{tr}}$ is the transmit complex weight of the n-th subcarrier at the m-th antenna. $\widetilde{W}_{n,m}^{\text{tr}}$ can further be expanded into polar form as

$$\widetilde{W}_{n,m}^{\text{tr}} = S_{n,m} e^{j\phi_{n,m}}, \tag{3.4}$$

where $S_{n,m} = |\widetilde{W}_{n,m}^{\text{tr}}| \geqslant 0$ and $\phi_{n,m} = \measuredangle\widetilde{W}_{n,m}^{\text{tr}} \in [0, 2\pi)$ represent the amplitude and phase of $\widetilde{W}_{n,m}^{\text{tr}}$, respectively. Then, the transmit signal over the wireless channel at time t on antenna m can be represented as

$$
\begin{aligned}
x_m^{\text{tr}}(t) &= \Re\left\{ \sum_{n=0}^{N-1} \sqrt{2}\widetilde{W}_{n,m}^{\text{tr}} e^{j2\pi f_n t} \right\} \\
&= \Re\left\{ \sum_{n=0}^{N-1} \sqrt{2}S_{n,m} e^{j\phi_{n,m}} e^{j2\pi f_n t} \right\},
\end{aligned} \tag{3.5}
$$

where the operator $\Re\{\cdot\}$ takes the real part of the operand. By using (3.5), the average RF power of all antennas combined is calculated as

$$P_{\text{RF}}^{\text{t}} = \sum_{m=1}^{M} \varepsilon\{x_m^{\text{tr}}(t)^2\}. \tag{3.6}$$

The transmit signal then propagates to the ER through the channel, influenced by its impulse response $\tilde{h}_{\text{m}}(t)$. We denote this channel impulse response in frequency, between the m-th antenna at the ET and the receiving antenna, on the n-th subcarrier, by

$$\widetilde{H}_{n,m} = A_{n,m} e^{j\varphi_{n,m}}, \tag{3.7}$$

where $A_{n,m}$ and $\varphi_{n,m}$ represent the amplitude and phase of the frequency response at frequency f_n and antenna index m. The received RF signal at the ER then becomes

$$y(t) = \Re\left\{ \sum_{m=1}^{M} \sum_{n=0}^{N-1} \sqrt{2}\tilde{H}_{n,m}^{\mathrm{tr}} \widetilde{W}_{n,m}^{\mathrm{tr}} e^{j2\pi f_n t} \right\}. \tag{3.8}$$

The signal model presented in this section serves a fundamental pillar for subsequent maximization of the harvested power. The derived equation for the received signal offers valuable insights into the characteristics of the WPT system, which allows for greater understanding of its performance. As we progress, we will use this signal model to design effective waveforms, in order to attain maximum WPT system performance.

3.2   Optimization Approach

Using the system model presented in the previous section, we can express the general waveform design optimization problem like in [18], accounting for the non-linear behaviours in both the ET and ER. The idea is to find the optimal waveform that maximizes the quantity z_{DC}, defined in (2.23), for a single user WPT system, presented in Figure 3.1. This gives the following optimization

$$\max_{\overline{\mathbf{W}}^{\mathrm{tr}}, \widehat{\mathbf{W}}^{\mathrm{tr}}} z_{\mathrm{DC}}(\overline{\mathbf{W}}^{\mathrm{tr}}, \widehat{\mathbf{W}}^{\mathrm{tr}}) \tag{3.9}$$

$$\text{s.t.} \sum_{m=1}^{M} \frac{1}{2T} \int_T \left(\frac{x_m^{\mathrm{tr}}(t)}{G} \cdot \left[\frac{1}{1 - \left(\frac{x_m^{\mathrm{tr}}(t)}{A_{\mathrm{s}}}\right)} \right]^{\frac{1}{2\beta}} \right)^2 dt \leqslant P_{\max}^{\mathrm{in}},$$

$$\sum_{m=1}^{M} \sum_{n=0}^{N-1} \overline{W}_{n,m}^{\mathrm{tr}^2} + \widehat{W}_{n,m}^{\mathrm{tr}^2} \leqslant P_{\max}^{\mathrm{tr}},$$

where it can be seen that z_{DC} is expressed as a function of $\overline{\mathbf{W}}^{\mathrm{tr}}$ and $\widehat{\mathbf{W}}^{\mathrm{tr}}$, which are matrices including all the weights $\overline{W}_{n,m}^{\mathrm{tr}}$, and $\widehat{W}_{n,m}^{\mathrm{tr}}$, which are the real and imaginary parts of the complex transmitted weights $\widetilde{W}_{n,m}^{\mathrm{tr}}$ that were introduced in (3.3). In the above, it can be noted that z_{DC} is being optimized over the waveforms only.

Finding the optimal solution to this problem has been done in [18], where they used a first order Taylor approximation of the above objective function and then solved it iteratively using SCP in combination with Barrier's method.

Figure 3.2 illustrates the working principle of the SCP algorithm. First, the initial weights are chosen according to the power constraints of (3.9). The optimization continues until the main algorithm, Algorithm 1, completes execution. Within each iteration of Algorithm 1, Algorithm 2 runs several times, and for each iteration of Algorithm 2, Algorithm 3 is executed a large number of times (see Appendix B for further details). This nature of the SCP algorithm, using nested loops, combined with the extensive execution of Algorithm 3, which is implemented using Newton's optimization method, requiring calculations of gradients and Hessians of the objective function through matrix operations, poses challenges
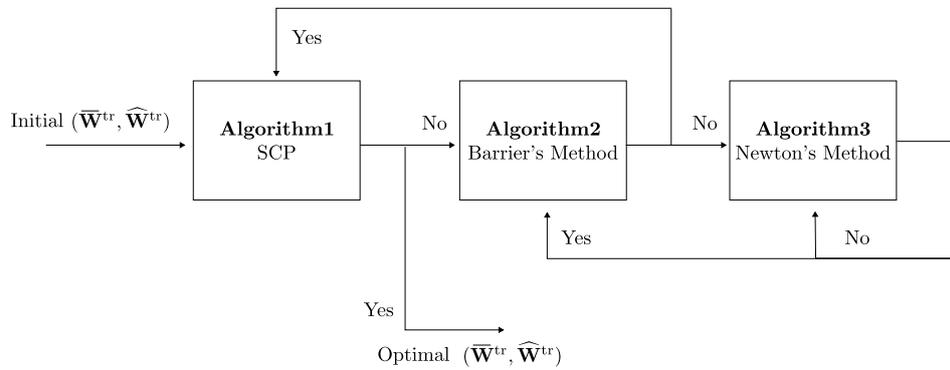
Figure 3.2: Block diagram of the SCP algorithm. The loop for each
algorithm continues until a required condition is fulfilled, repre-
sented by Yes. If the condition is not fulfilled, it is represented
by No.

in terms of computational complexity. This highlights the main weakness of using
SCP for problems with a large number of antennas or subcarriers, since the num-
ber of iterations required, and the computational time per iteration, quickly gets
out of hand.

3.3   Waveform Design for a Large Number of Antennas and Subcarriers

In a WPT system with a large number of antennas and subcarriers, we consider that the number of antennas can go up to 256, and the number of tones can reach several thousands, mainly when dealing with LIS and cellular networks. Due to the complexity growth discussed in the previous section, performing SCP optimization becomes infeasible for such large numbers of antennas and subcarriers. As an alternative, we use MRT for the waveform design when dealing with a large number of antennas and subcarriers. MRT has been extensively studied in the context of WPT in various papers [15,17]. Nevertheless, the existing literature has primarily investigated MRT for WPT under the assumption that the transmitter maintains a constant efficiency in the waveform that is being transmitted. In this section, we present waveform design based on MRT, but we take into account non-linearity at both the ET and ER.

3.3.1   Maximum Ratio Transmission

MRT is a technique used in wireless communication systems to optimize signal transmission from multiple antennas to a receiver. It employs the concept of maximizing the received signal power by adjusting the weights of the antennas based on the CSI [14].

The input weights according to MRT are chosen as

$$\widetilde{W}_{n,m}^{\mathrm{in}} = \sqrt{P_{\mathrm{total}}^{\mathrm{in}}} \cdot \frac{H_{n,m}^*}{\|\mathbf{H}\|}, \tag{3.10}$$

where $P_{\mathrm{total}}^{\mathrm{in}} = \sum_{m=1}^{M} P_{\mathrm{RF,m}}^{\mathrm{in}}$ denotes total input power used in the M PAs at the ET, and $P_{\mathrm{RF,m}}^{\mathrm{in}}$ denotes the input power to the m-th PA. This shows that CSI, $H_{n,m}$, is needed to make sure that the signals add up in phase at the input of the ER. Furthermore, it can also be seen that MRT performs power allocation where strong sub-channels get more power, and weak sub-channels get less power. It is important to note that the weights used are the input weights, not the transmitted weights. These input weights create input signals $\tilde{x}_m^{\mathrm{in}}(t)$ by the relation in (3.1). These input signals will be amplified and may experience distortion by the power amplifiers, resulting in the amplified weights, $\widetilde{\mathbf{W}}_{n,m}^{\mathrm{PA}}$, that form the amplified signals $\tilde{x}_m^{\mathrm{PA}}(t)$. The distortion significantly impacts the efficiency at the ET, leading to an increase in the power loss between the input and output power of the amplifiers. Therefore, when selecting input weights using MRT, it is crucial to carefully consider the distortion level to ensure efficient and effective power transfer. In the following subsection, we introduce a measure of the distortion level and propose a method to mitigate it in order to ensure end-to-end efficiency.

3.3.2   Out-of-band Emission and Power Back-off

Out-of-band (OOB) emission, as described in Subsection 2.3.2, refers to unwanted signals transmitted at frequencies outside an allowed bandwidth in a wireless system. To consider the efficiency of the WPT system and evaluate e_1, measuring the

OOB power level, which is the difference between the power of frequency components within the allowed bandwidth and those outside of it, serves as an effective metric. We have chosen to represent the OOB power level of m-th PA as

$$\mathrm{OOB}_m = \varepsilon\big\{|\widetilde{W}^{\mathrm{PA}}_{n^{\mathrm{out}},m}|^2\big\}_{\mathrm{dB}} - \varepsilon\big\{|\widetilde{W}^{\mathrm{PA}}_{n^{\mathrm{in}},m}|^2\big\}_{\mathrm{dB}}, \tag{3.11}$$

where the subscripts n^{in} and n^{out} indicate the subcarrier indices for in-band and out-of-band frequencies, respectively. Figure 3.3 shows an example of a high peak signal passing through a PA at the ET. The scenario considers an OFDM signal with $N = 1200$ tones as the input signal and a single transmit antenna, $M = 1$ at the ET. As shown in Figure 3.3a, the input signal has significant peaks that extend beyond the saturation voltage, A_{s}, of a PA. When this signal passes through a PA, the peaks that exceed A_{s} experience soft clipping, resulting in signal distortion, as illustrated in Figure 3.3b. Figure 3.4 shows the frequency responses of two signals in Figure 3.3. By examining Figure 3.4a and Figure 3.4b, we can observe that the frequency responses of the distorted signal spread over the allowed bandwidth, leading to OOB power level of -13.18 dB. This value is higher than what is typically allowed in cellular networks, where the level is usually between -30 to -50 dB.

One approach to decreasing the OOB power level is to use IBO, which involves reducing the amplitude of the input signal peaks as discussed in Section 2.3. However, when dealing with a large number of antennas, such as LIS, evaluating M different $\mathrm{P}^{\mathrm{OOB}}_m$ and applying individual IBO to each amplifier will be challenging. Instead, we propose a practical solution by evaluating the average OOB power level over all antennas to describe the overall OOB level of the ET with multiple antennas, denoted as

$$\mathrm{OOB} = \varepsilon\big\{\mathrm{OOB}_m\big\}, \tag{3.12}$$

where $\varepsilon\{\cdot\}$ denotes the expectation operator over antennas. Then, we estimate a corresponding total input power back-off (TIBO) to meet the required power level. Subsequently, the total input power after applying TIBO becomes

$$P^{\mathrm{in,TIBO}}_{\mathrm{total}} = P^{\mathrm{in}}_{\mathrm{total}} - \mathrm{TIBO} \ [\mathrm{dB}]. \tag{3.13}$$
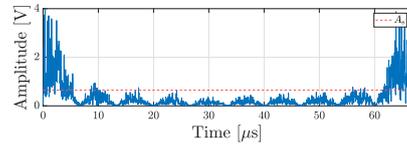
(a) A signal before passing through a PA.
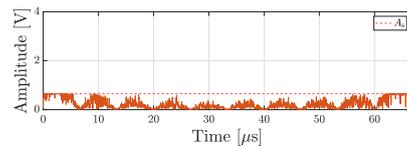
(b) A distorted signal after passing through a
PA.

Figure 3.3: High peak OFDM signal before and after passing
through a PA. The signal is created by using MRT where $M = 1$
antenna and $N = 1200$ tones.
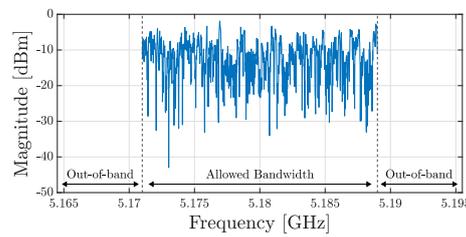
(a) Frequency response of a signal before passing
through a PA.
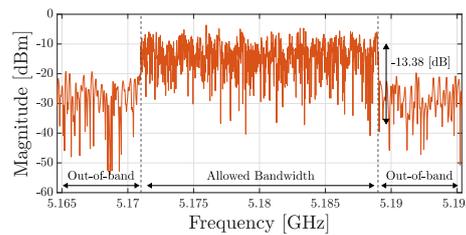
(b) Frequency response of a distorted signal after
passing through a PA.

Figure 3.4: Frequency responses of a high peak signal before and
after passing through a PA, where $M = 1$ antenna and $N =
1200$ tones.

3.3.3   Simulation Framework

Let us now take a look at the simulation framework that has been implemented using MATLAB for the investigation of the MRT waveform design. The block diagram in Figure 3.5 shows all the different steps.

At the ET, firstly, we decide on the total input power and choose the input weights, $\widetilde{\mathbf{W}}^{\mathrm{in}}$, with M antennas and N tones, by using MRT, based on the CSI according to (3.10). Afterward, the input weights are transformed into the time domain by performing Inverse Fast Fourier Transform (IFFT) creating the complex input baseband signal[1], $\tilde{x}_{\mathrm{bb}}^{\mathrm{in}}[k]$. To sample the baseband signal, we approximate that its frequency components are limited to within the range of $[0, f_{\mathrm{bb}}^{\mathrm{max}}]$, where $f_{\mathrm{bb}}^{\mathrm{max}} = \kappa N \Delta_s$. Here, κ denotes the upsampling coefficient, and Δ_{s} is the subcarrier spacing. Then, the sampling frequency is set at $2\kappa N \Delta_s$ based on the Nyquist sampling theorem. Consequently, $k = 0, ..., 2\kappa N - 1$, denoting the index of the discrete baseband time signal. Then, the SSPA model is applied to simulate the PA's non-linearity, resulting in the complex amplified baseband signal, $\tilde{x}_{\mathrm{bb}}^{\mathrm{PA}}[k]$. Fast Fourier Transform (FFT) is then performed on this signal to obtain the amplified weights, $\widetilde{\mathbf{W}}^{\mathrm{PA}}$. Next, OOB power level is evaluated based on the in-band and out-of-band frequency responses of $\widetilde{\mathbf{W}}^{\mathrm{PA}}$. If the OOB level does not meet the required level set in the system, the necessary TIBO is calculated to meet the condition. The total input power of the system is adjusted accordingly, and the process is repeated. If the OOB level meets the requirement, the amplified weights go through an ideal BPF [2] that selects only the weights inside the allowed bandwidth. This filtering process results in the complex transmitted weights denoted as $\widetilde{\mathbf{W}}^{\mathrm{tr}}$.

Now, $\widetilde{\mathbf{W}}^{\mathrm{tr}}$, which are designed at the ET, pass through a propagation channel, resulting in the complex received baseband signal, $\tilde{y}_{\mathrm{bb}}[k]$. Finally, to assess the performance of the designed waveform, the output DC current, $\bar{i}_{\mathrm{out}}$ is calculated by using (2.16).

---

[1] In our system, we choose to sample the baseband signal instead of directly sampling the RF signal as it offers the advantage of quicker simulations. To avoid aliasing, the sampling frequency of the bandpass signal should be higher than $f_c + \mathrm{BW}/2$. However, this results in a large number of samples, requiring higher computational resources for processing.

[2] One might be concerned that implementing an ideal BPF is impractical. Indeed, implementing an ideal BPF with perfect frequency selectivity is challenging in practice due to various real-world limitations. However, by applying TIBO and reducing the OOB power level before the BPF, the impact of out-of-band frequency components is significantly mitigated. This makes the approximation of the ideal BPF feasible, ensuring sufficient out-of-band signal suppression.
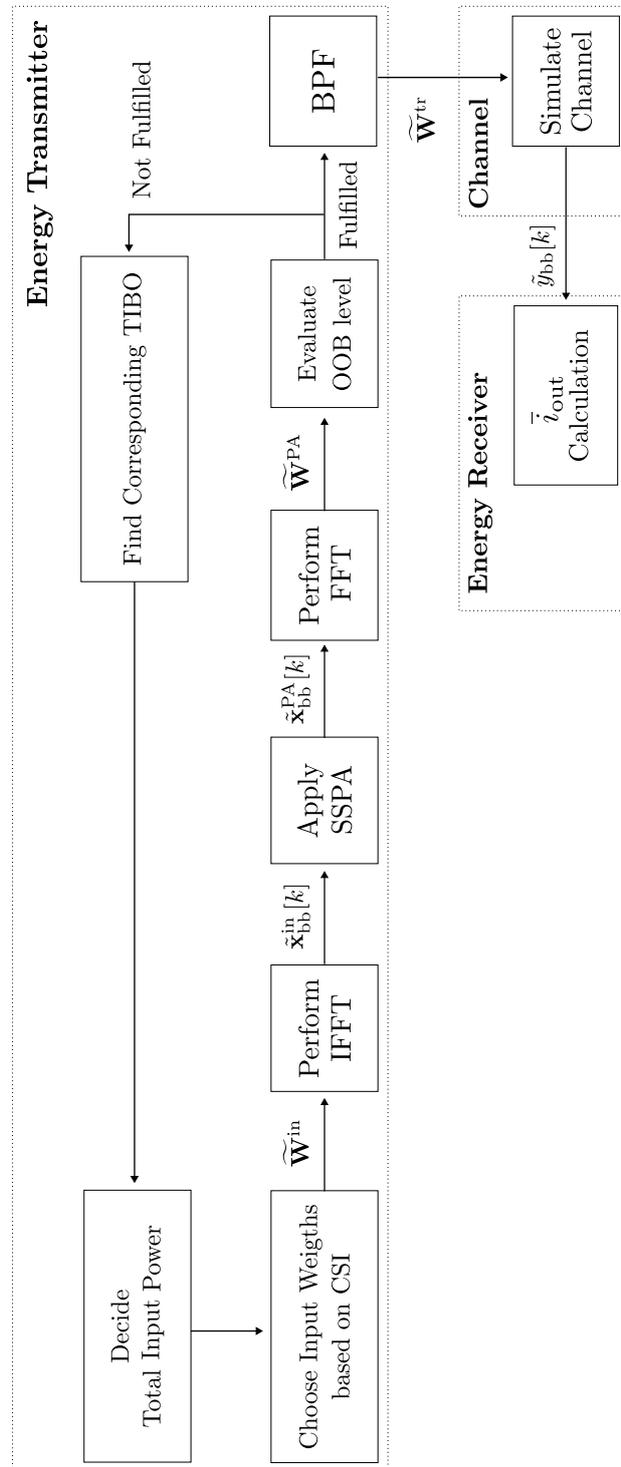
Figure 3.5: Block diagram of the MRT simulation.

Based on the simulation framework described, the focus will now shift to presenting the simulation results in the upcoming chapter.

Simulation Results

This chapter presents the simulation results of the two waveform design approaches based on SCP optimization and the MRT scheme described in the previous chapter. Section 4.1 describes the parameter settings used in our simulations. In Section 4.2, we show the performance of optimal waveforms achieved by the SCP algorithm. In Section 4.3, we present and analyze simulation results focusing on the use of MRT as a feasible solution in scenarios with a large number of antennas, where we provide a better understanding of the resulting performance for different parameter sets and channel conditions.

4.1   Parameters Settings and Simulation Assumptions

Our simulation framework concerns a cellular network environment, using the parameters outlined in Table 4.2. To demonstrate the impact of the antenna array at the ET, we systematically vary the number of transmit antennas up to $M = 256$. Furthermore, we adjust the values of the SSPA parameter, β, to observe the effects of varying the amplifier quality. For the ER, we use a single receiving antenna, with an antenna resistance, R_{ant}, of 50, assuming perfect matching with the input resistance $R_{\mathrm{in}} = 50\Omega$. Additionally, we follow the diode parameters specified in the SMS-7630 datasheet, where v_{t} is at 25.86 mV assuming room temperature. The resistance of the load, R_{L}, is set to 20 kΩ.

For our channel parameters, we set the carrier frequency, f_{c}, to be 5.18 GHz with pathloss at -56 dB. We place subcarriers in an allowed bandwidth of 20 MHz, centered within the total bandwidth of 30.72 MHz, while the remaining bandwidth serves as guard bands. OFDM is employed, with the number of used tones N as equally spaced subcarriers across the allowed bandwidth to achieve a high peak signal. The frequency of the nth subcarrier, denoted as f_n, follows the equation $f_n = f_0 + (n-1) \cdot \Delta_{\mathrm{s}}$, where f_0 represents the frequency of the lowest subcarrier, and Δ_{s} denotes subcarrier spacing. Δ_s is set to 15 kHz, where 1200 represents the maximum number of subcarriers within the 20 MHz bandwidth. Furthermore, we set the limit on the number of selected tones, $N^{\mathrm{lim.}}$, to 20 to prevent a reduction in harvester efficiency, thereby adhering to the specified PAPR limit in (2.24). By considering our load and antenna resistance values, we deduce from (2.24) that the PAPR should be maintained below 40. Through MATLAB simulations, we have observed that a PAPR below 40 is attainable for N values below 20. The

31

spacing between used tones is calculated as $\left\lfloor \frac{1200}{N} \right\rfloor \cdot 15$ kHz, where used N tones are equally spaced in the bandwidth.

Furthermore, we conducted simulations employing diverse channel models, each characterized by unique correlation attributes, to examine the influence of channel correlation on WPT performance. The Independent and Identically Distributed (IID) Rayleigh channel is frequently used in practice. This channel assumes that the random fading process is statistically independent and maintains an identical distribution across antennas and subcarriers. It serves as a widely adopted and fundamental representation of propagation channel characteristics. However, it may not capture the intricacies of realistic channel properties. In addition to the IID channel, we integrate four additional channel models, each described as follows:

— Rayleigh channel with correlation across both antennas and subcarriers

— Rayleigh channel with correlation across only subcarriers

— Rayleigh channel with correlation across only antennas

— Propagation channel in the free-space environment

Firstly, for the **Rayleigh channel with correlation across both antennas and subcarriers**, we assume that each antenna and subcarrier correlates with its 10 closest neighbors. This specific channel model is used as a benchmark for evaluating the performance of WPT, offering a moderate level of correlation. It serves as a reference point for comparison against the subsequent two highly correlated channel models.

Additionally, we introduce a **Rayleigh channel with correlation across only subcarriers** to demonstrate a correlation among different frequency components. Within this configuration, we assume that each subcarrier is correlated with its 100 nearest neighboring subcarriers. Similarly, for a **Rayleigh channel with correlation across only antennas**, we assume that each antenna is correlated with its 10 nearest neighboring antennas. This representation captures the concept of antenna-correlated channels.

Lastly, we incorporate **a propagation channel in the free-space environment**. This channel model assumes a scenario occurring in an unobstructed free-space path between the transmitter and receiver. Within this setup, both antennas and subcarriers are fully correlated. Figure 4.1 illustrates the attenuation of the five introduced different channels, providing a graphical understanding of their distinct correlation characteristics. The depicted scenarios use a path loss of 56 dB, 1200 tones ($N = 1200$), and 128 antennas ($M = 128$).
Remark: We apply all of the different channel models mentioned in this subsection for MRT, whereas for the SCP, we limit ourselves to the IID Rayleigh channel.

Channel	SCP	MRT
IID channel	✓	✓
Correlation across antennas and subcarriers	-	✓
Correlation across only subcarriers	-	✓
Correlation across only antennas	-	✓
Free-space channel	-	✓

Table 4.1: Simulated Channel Scenarios.

Now that we have described the simulation assumption and parameter settings, let us move on to the simulation results of the two waveform designs in the framework.

Component		Parameter	Value	Unit
Energy Transmitter (ET)	Antenna	Number of Antennas, M	$1,...,256$	-
	SSPA	Smoothing Factor, β	$1, 3, 5$	-
		Saturation Voltage, A_{s}	$0.875, 10$	V
		Gain, G	1	-
Energy Receiver (ER)	Antenna	Number of Antennas	1	-
		Antenna Resistance, R_{ant}	50	ohm
		Reverse Bias Saturation Current, I_{s}	5	μA
		Diode Breakdown Saturation Current, I_{BV}	10	mA
	Rectifier and LPF	Ideality Factor, η	1.05	-
		Breakdown Voltage, v_{br}	2	V
		Thermal Voltage, v_{t}	25.86	mV
		Load Resistance, R_{L}	2000	Ohm
Channel and OFDM Signal	Channel	Carrier Frequency, f_c	5.18	GHz
		Pathloss	-56	dB
	OFDM Signal	Total Bandwidth	30.72	MHz
		Allowed Bandwidth	20	MHz
		Subcarrier Spacing, Δ_{s}	15	kHz
		Number of Tones, N	$1,...,20$	-
		Used Subcarrier Spacing	$\lfloor \frac{1200}{N} \rfloor \cdot 15$	kHz

Table 4.2: Summary of parameters within the system framework.

4.2   SCP Optimization

In this section, we present the simulation outcomes from the SCP optimization, which we described briefly in Section 3.2 as one of our waveform design approaches. Through these results, we study the impact of both the number of antennas and tones on the performance of z_{DC}. Additionally, we analyze how the SCP optimization allocates power across optimized transmitted weights, providing a better understanding of the chosen waveform design for increasing z_{DC} performance.

In the following, we will analyze the performance of the SCP algorithm while varying the number of antennas and tones. Due to the algorithm's complexity, we will limit the size of variables to small values, with the number of antennas, M, and the number of tones, N, set to a maximum of 8.

4.2.1   Influence of Number of Antennas

In this subsection, we analyze the z_{DC} performance as a function of maximum transmit power for the different number of antennas and a certain number of tones.

Figure 4.2 shows us the z_{DC} performance for the antenna number, M, equals to 1, 2, 4, and 8 and when the number of tones, N, is set to 2. In the figure, we see how z_{DC} changes for different transmit antenna configurations. As expected, a higher number of antennas results in better performance. This is mainly for two reasons: *i)* A higher number of antennas leads to a higher array gain which increases the RF-RF efficiency leading to a higher power level at the input of the receiver. *ii)* we see that as the number of antennas increases, the value at which z_{DC} converges and becomes constant increases. This is because a higher number of antennas is equivalent to increasing the number of transmit chains, leading to the total transmitted power being distributed over a higher number of transmitter amplifiers. Because of this, the signal going through the individual amplifiers at the ET have lower powers for setups with a higher number of antennas, which makes these amplifiers operate further away from their saturation voltages, allowing for convergence at a higher maximum transmit power.

4.2.2   Influence of Number of Tones

We move on to study the z_{DC} performance as a function of maximum transmit power for the number of tones, N, equal to 1, 2, 4, and 8, and when the number of antennas, M, is set to 2 in Figure 4.3. Here, we see a higher number of frequency tones gives better z_{DC} performance. However, this is not as dramatic as the improvement we witnessed with increasing the number of antennas. The increase in z_{DC} performance for the higher number of tones is explainable because as the number of tones increases, the received signal gets a higher PAPR. A higher PAPR leads to a more peaky signal, so more of the power is concentrated in the non-linear region of the diode. This means that a higher number of tones gives better efficiency at the receiver. With this information, one may think that we have to transmit in as many tones as possible. However, after a threshold, the diode will eventually enter its breakdown region, leading to a saturated level of z_{DC} even

(a) IID channel.

(b) Correlation across antennas/subcarriers.

(c) Correlation across only subcarriers.

(d) Correlation across only antennas.

(e) Free-space channel.
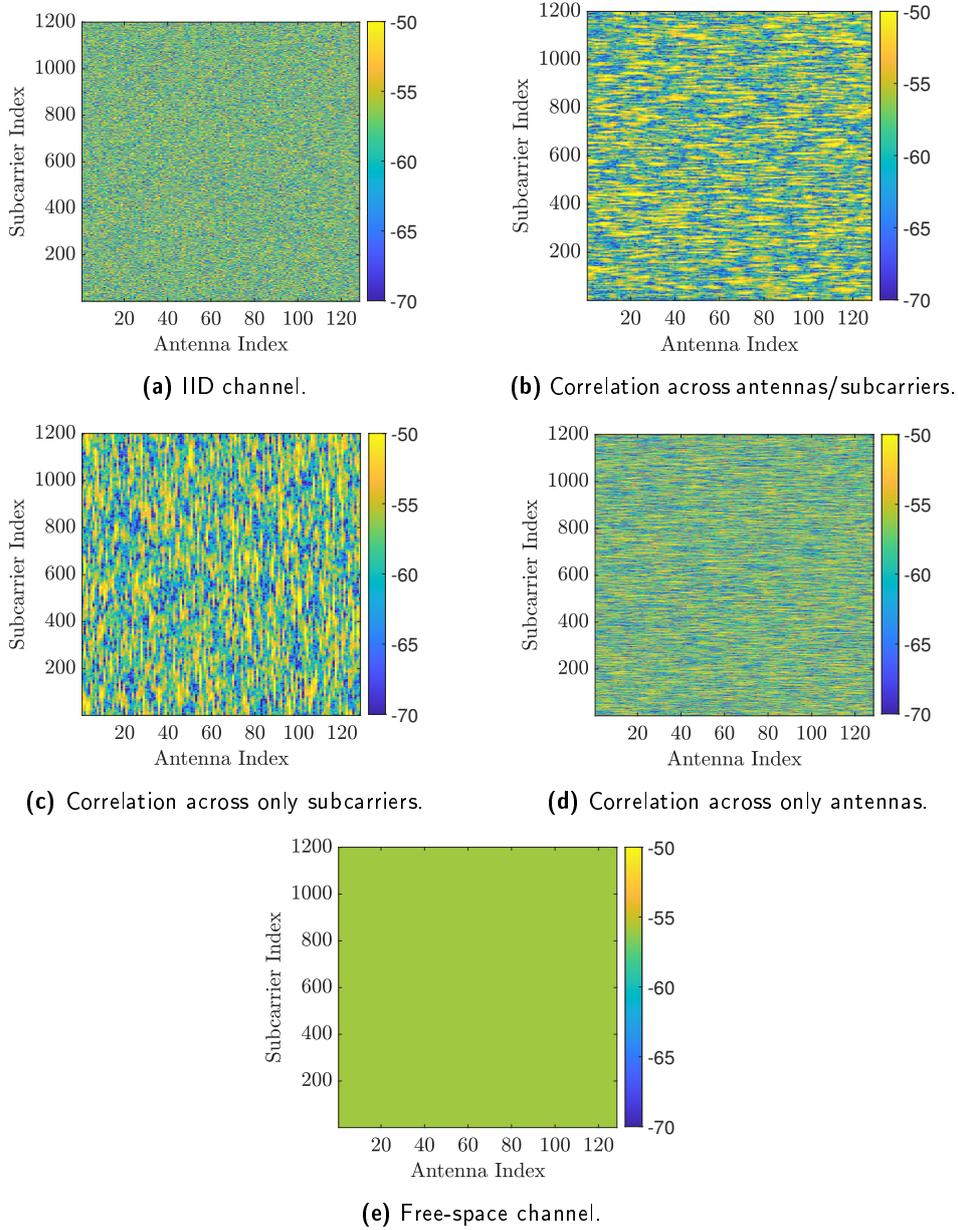
Figure 4.1: Attenuation of different Rayleigh channels with $N = 1200$ tones and $M = 128$ antennas. The color bars are in dB scale. To improve visibility, the attenuation range is [-70, -50] dB, even though the Rayleigh channel exhibits a larger variation. This is done by assigning a consistent color (dark blue) for values of -70 dB or below and another (yellow) for values of -50 dB or above.
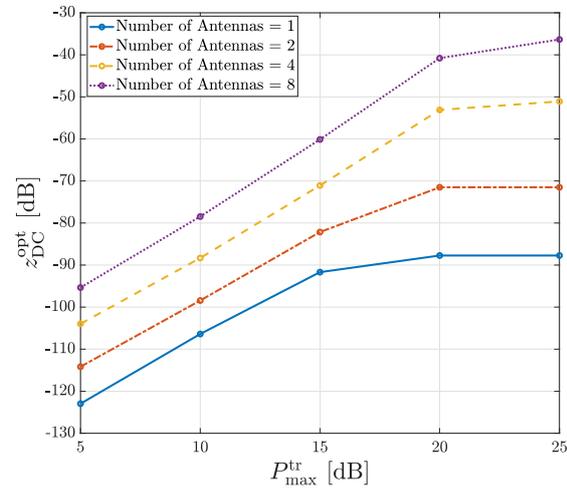
Figure 4.2: z_{DC} as a function of maximum transmit power for the different number of antennas when the number of tones, N, is set to 2.
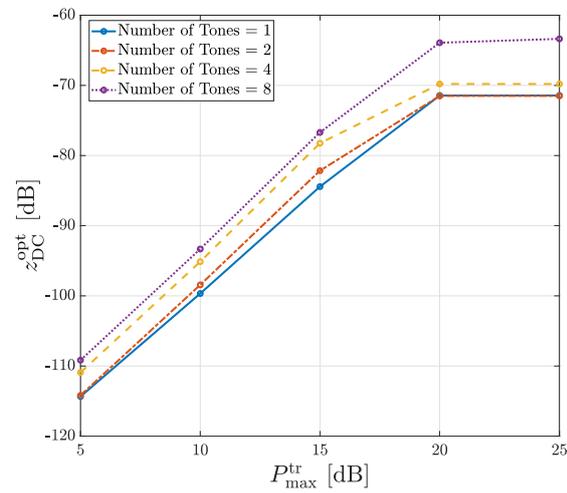
Figure 4.3: z_{DC} as a function of maximum transmit power for the different number of tones when the number of antennas, M, is set to 2.

with higher power and peak levels. This phenomenon reduces the efficiency of the rectifier, as discussed in [17].

4.2.3   Power Allocation of Waveforms Optimized by SCP

While we have inspected the influence of increasing the number of antennas and tones on the z_{DC} performance, the current set of results may not provide a conclusive understanding due to the configuration being limited by the complexity of the algorithm. Here, we analyze the optimized transmitted weights achieved through SCP in this subsection. This is to better understand the strategy of optimal waveform design and provide suggestions for designing waveforms for systems with larger number of antennas or tones.

Our analysis focuses on investigating the power distribution of the optimized waveform across various subcarriers and antennas. This is achieved by comparing each weight with its corresponding channel coefficient. In Figure 4.4, the power allocation of the optimized transmit weights is shown with the channel coefficient where we set the number of tones, N, and antennas, M, as follows: 2 tones and 4 antennas, 4 tones and 4 antennas, and 8 tones and 2 antennas. In this visualization, the maximum transmit power is set to 15 dB so that the signals at the ET do not experience significant distortion by PAs. Upon inspecting the figure, it becomes evident that power distribution across antennas and subcarriers differs from the channel strengths. Notably, the behaviour of the SCP algorithm exhibits similarity to MRT, as stronger sub-channels get higher power allocations than weaker sub-channels. In conclusion, our investigation suggests that integrating MRT into waveform design can be a practical approach for enhancing z_{DC} performance. Furthermore, this finding enables a more extended analysis involving a larger number of antennas and tones, alleviating the complexity associated with the SCP algorithm.

(a) $\widetilde{\mathbf{W}}_{\mathrm{opt}}^{\mathrm{tr}}$ for 2 tones and 4 antennas.

(b) $\tilde{\mathbf{H}}_{\mathrm{IID}}$ for 2 tones and 4 antennas.

(c) $\widetilde{\mathbf{W}}_{\mathrm{opt}}^{\mathrm{tr}}$ for 4 tones and 4 antennas.

(d) $\tilde{\mathbf{H}}_{\mathrm{IID}}$ for 4 tones and 4 antennas.

(e) $\widetilde{\mathbf{W}}_{\mathrm{opt}}^{\mathrm{tr}}$ for 8 tones and 2 antennas.

(f) $\tilde{\mathbf{H}}_{\mathrm{IID}}$ for 8 tones and 2 antennas.

Figure 4.4: Power allocation of optimized transmit weights obtained by SCP, $\tilde{\mathbf{H}}_{\mathrm{IID}}$, and the corresponding attenuation of IID Rayleigh channel, $\tilde{\mathbf{H}}_{\mathrm{IID}}$. $P_{\mathrm{max}}^{\mathrm{tr}} = 15$ dB. The color bars are in dB scale.
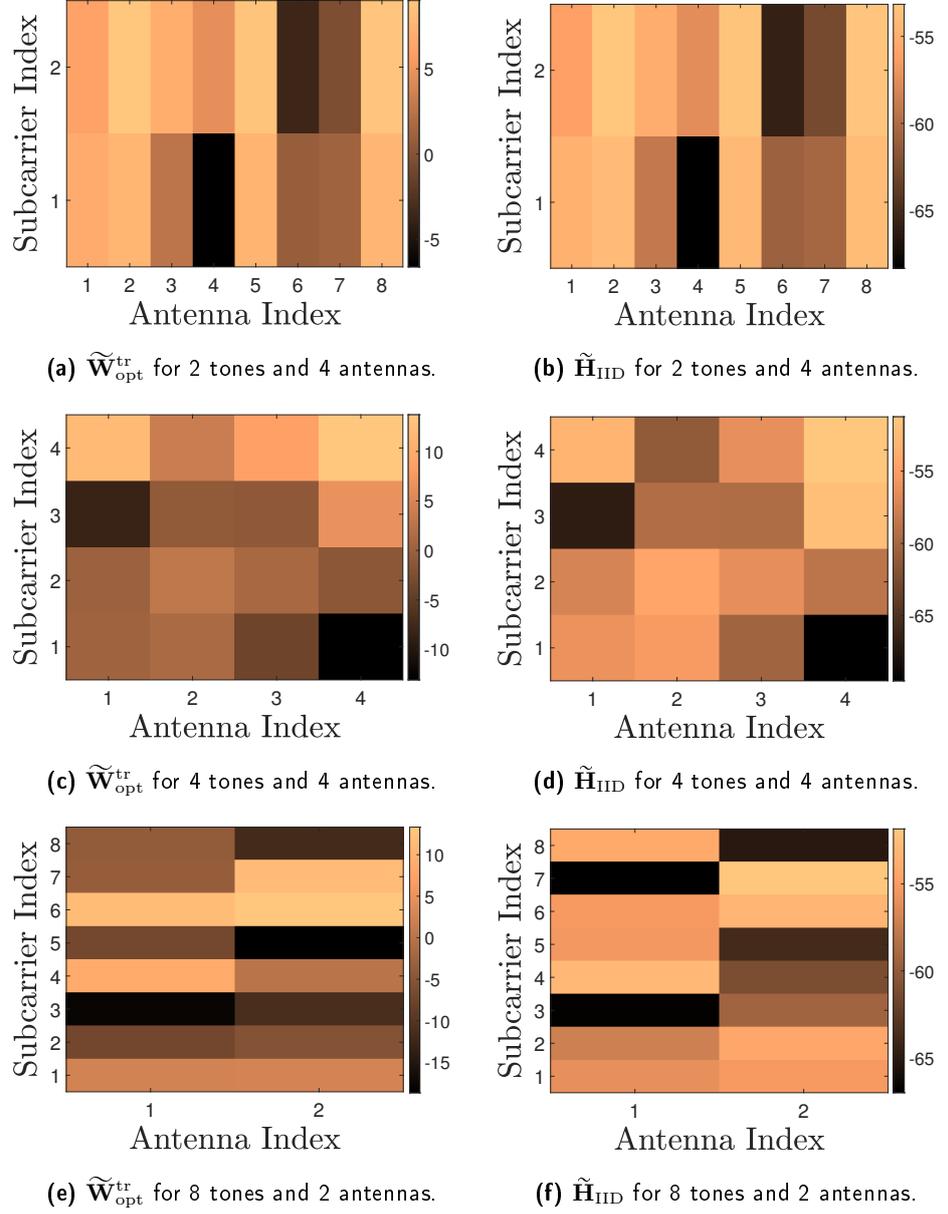
4.3   MRT and Large Number of Antennas

This section presents simulation results using MRT for our waveform design. Considering that the MRT operation in (3.10) is executed only once per channel realization, the computational complexity for waveform design is significantly reduced compared to the SCP optimization. This reduction in complexity allows for a larger number of antennas and tones to be used. Therefore, we extended the number of antennas, M, up to 256 and the number of tones, N, up to 20 − the upper limit for the number of tones.

The purpose of these simulations is to evaluate the performance of harvested DC output current at the ER. Since we incorporate the scaled-up antenna number, leveraging an array gain by a factor of the number of antennas, the assumption of a significantly small received signal for using z_{DC} is no longer applicable. Instead, we directly evaluate the DC output current, i_{out} at a rectifier using (2.16). In the following subsections, we analyze the i_{out} performance for the number of tones, scaled-up antenna number, PA qualities, and different channel correlations. Moreover, to account for the efficiency at the ET, we assess the average OOB power level, OOB, and implement a total input power back-off, TIBO, when the associated OOB surpasses a certain level of regulation threshold, i.e., -40 dB in our setup. The analysis of i_{out}^{TIBO} across different parameter values provides a better understanding of our system's behaviour in various scenarios.

4.3.1   Influence of Number of Tones

In this subsection, we focus on the investigation of the i_{out} performance with respect to the total input power, P_{total}^{in}, for varying number of tones. P_{total}^{in} is used to generate input weights using MRT. The parameter configuration includes $M = 128$ antennas, $\beta = 3$, and the average correlated channel in Figure 4.1(b). Additionally, we examine the associated OOB levels with the number of tones.

Figure 4.5 shows the i_{out} performance for different numbers of tones: 2, 4, 8, 16, and 20, for the specified parameter configuration. As observed in the figure, i_{out} increases more rapidly with a higher number of tones. This trend aligns with the observations made in the previous section regarding z_{DC} with varying the number of tones. It is worth highlighting that i_{out} also demonstrates improved performance for a higher number of tones, up to the defined limit. However, all the curves eventually saturate at the same level, indicating the attainment of the maximum achievable DC current. This saturation point is reached when the rectifier starts suffering from diode breakdown.

To provide more analysis on the impact of the number of tones on the i_{out} performance, we can examine the average power of the received signal to achieve saturation, along with the corresponding PAPR. Figure 4.6 shows the relationship between received power and the corresponding PAPR as a function of the number of tones. The result demonstrates that higher PAPR values are associated with lower required P_{total}^{in} to achieve saturation. Specifically, when the number of tones, N, is 20, the received power measures -31.18 dB, corresponding to a high PAPR of 38.24 in the received signal. This reflects a significantly lower power level compared to the scenario where the number of tones is 2, and the required P_{total}^{in} is -22.63

Figure 4.5: i_out as a function of total input power for different number of tones. Parameter configuration: $M = 128$ antennas, $\beta = 3$, and the average correlated channel in Figure 4.1(b).

dB, with a much lower PAPR of 3.96 in the received signal. As a result, it becomes evident that a higher number of tones leads to a higher peak signal, which enhances the performance of i_out at the ER. Conversely, as previously discussed, a higher
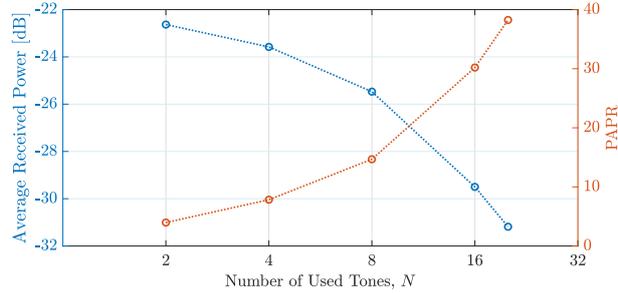
Figure 4.6: The necessary received power and PAPR required to achieve saturation as a function of the number of tones. The blue dotted curve shows the average received power, and the red dotted curve shows the corresponding PAPR of received signals.

peak signal can affect the efficiency of the ET, resulting in increased distortion introduced by the PAs. Figure 4.7 illustrates that the growth of OOB becomes more pronounced for higher number of tones, N. As N increases, the higher peak signal easily surpasses the linear operating region of the PAs, leading to an increase in distortion.

In the analysis of the results, we have observed that higher peak signals allow us to achieve improved performance at the ER. However, it is essential to know that higher peak signals also introduce increased distortion, leading to higher OOB and decreased efficiency of the ET. To address this issue, we have proposed the
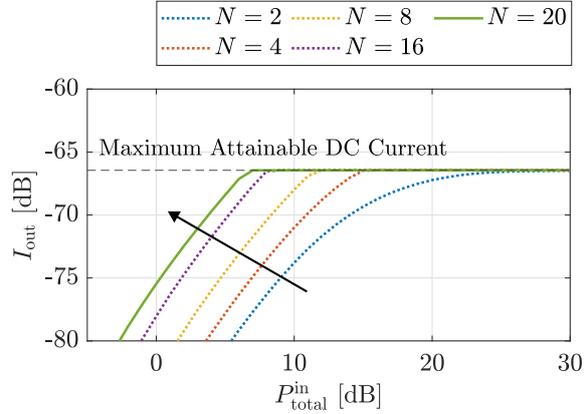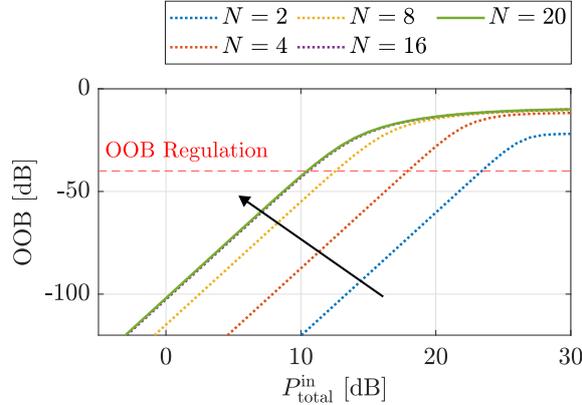
Figure 4.7: P^{OOB} as a function of total input power for different number of tones. Parameter configuration: $M = 128$ antennas, $\beta = 3$, and the average correlated channel in Figure 4.1(b).

implementation of TIBO to mitigate distortion and while retaining the end-to-end efficiency.

In the following subsection, we aim to investigate the influence of the number of antennas in scenarios with a large number of antennas. We will consider all aspects, including the impact of higher peak signals on i_{out} performance, the requirement for TIBO to meet the OOB regulation, and the potential benefits of using multiple antennas to enhance system performance.

4.3.2 Scaling up Number of Antennas

Now, we study the performance of i_{out} for varying number of antennas, M, considering the end-to-end efficiency. With the configuration on the number of tones, N, equals to 2, 4, 8, 16, and 20, with $\beta = 3$ and the average correlated channel in Figure 4.1(b), we mainly demonstrate the following aspects: *i)* the influence of the number of antennas on i_{out} and OOB as a function of the total input power. *ii)* the required TIBO level at the saturation points of the rectifier and apply TIBO to understand the attainable DC current considering the end-to-end efficiency, $i_{\mathrm{out}}^{\mathrm{TIBO}}$, and the corresponding input power, $P_{\mathrm{total}}^{\mathrm{in,TIBO}}$. Additionally, for cases where OOB is lower than the OOB regulation, we provide further understanding into the increase in the distance that a device is charged in our system.

Figure 4.8 shows the behaviour of i_{out} as a function of the total input power, $P_{\mathrm{total}}^{\mathrm{in}}$, along with the corresponding OOB, where the number of antenna, M, is equal to 64,128, and 256. Here, let us consider two cases where the number of tones, N, equals 2 and 20. The "*" marker in Figure 4.8 indicates the saturation point, which is driven either by the breakdown of the rectifier at the ER, reaching the maximum attainable DC current, or by the non-linearity of the PAs limiting the transmit power level.

In the figure, it can be noted that i_{out} exhibits a more rapid increase with higher values of M. This behaviour can mainly be attributed to two reasons. First,

increasing the number of antennas makes the power across them more distributed, leading to lower input signal levels for the PAs. Consequently, OOB in the PAs can be reduced, allowing the PAs to operate in a more linear region. This decrease in OOB results in reduced distortion and improved performance. The blue dotted line in Figure 4.8(a, left) shows the impact of the PAs' non-linearity on i_{out} in a scenario with a relatively small number of antennas, $M = 64$, and a small number of tones, $N = 2$. This scenario requires higher $P_{\text{total}}^{\text{in}}$ to reach saturation, and the saturation DC current is 8.74 dB lower than the maximum current due to the non-linearity of the PAs. However, as the number of antennas increases, this effect is mitigated. With more antennas, the system requires a lower $P_{\text{total}}^{\text{in}}$ level to reach saturation, and a higher saturated DC current is achieved. Figure 4.8(a, right) shows that the corresponding OOB is also mitigated by increasing the number of antennas. This demonstrates the advantages of using a larger number of antennas in improving system efficiency and reducing OOB emissions caused by the PAs' non-linearity.

Another reason for the different i_{out} performance concerning the number of antennas is the associated array gain achieved by implementing MRT. In Figure 4.8 (b, left), where the number of tones is 20, and the required input power level is low, we can avoid the non-linear effects of the PAs, thereby showing the variations mainly attributable to the array gain. As we double the antenna number, the gain between the curves is approximately 3 dB, as expected based on $10 \log(M)$, demonstrating the benefits of array gain in enhancing i_{out} performance.

However, it is worth noting that specific saturation points marked with '*' on the figure surpass the OOB regulation. As we have previously discussed, higher levels of OOB indicate increased distortion, which ultimately reduces the efficiency of the ET. To maintain the desired efficiency, we systematically apply TIBO. For instance, considering the blue dashed curve in Figure 4.8 (b, right) with $P^{\text{OOB}} = -20.32$ dB, TIBO of 5 dB is introduced to meet the regulation. As a result, the adjusted total input power becomes $P_{\text{total}}^{\text{in,TIBO}} = 7$ dB, resulting in a resultant $i_{\text{out}}^{\text{TIBO}} = -70.98$ dB, which is 11.53 dB lower than the maximum DC current. This value represents the DC output current considering the end-to-end efficiency. By extending these steps to all scenarios, Figure 4.9 presents an overview of the overall $i_{\text{out}}^{\text{TIBO}}$, the required TIBO level, and $P_{\text{total}}^{\text{in,TIBO}}$ for various number of tones and antennas. The figure mainly shows that smaller values of M require greater TIBO, resulting in lower $i_{\text{out}}^{\text{TIBO}}$ for our system.

Now, let us focus on the scenarios with $M = 128$ antennas and $M = 256$ antennas. We observe that we are already adhering to the OOB regulation without any TIBO, except for $M = 128$ antennas with $N = 2$ tones. This provides an even larger margin to increase the input power up to the OOB regulation. The extra margin gained can be used to improve the system's transmission capabilities. By increasing the input power at the ET, we can adjust the OOB level to fall on -40 dB. This additional input power can then increase the distance we can charge the device, thereby enhancing the system's overall range and coverage. Figure 4.10 illustrates the additional $P_{\text{total}}^{\text{in}}$, corresponding extra margin, and the extra distance we can gain for the number of antennas and tones, calculated based on a free-space assumption. As expected, the figure highlights that a larger number of antennas leads to greater extra distance, reaching up to $+205\%$ additional distance where
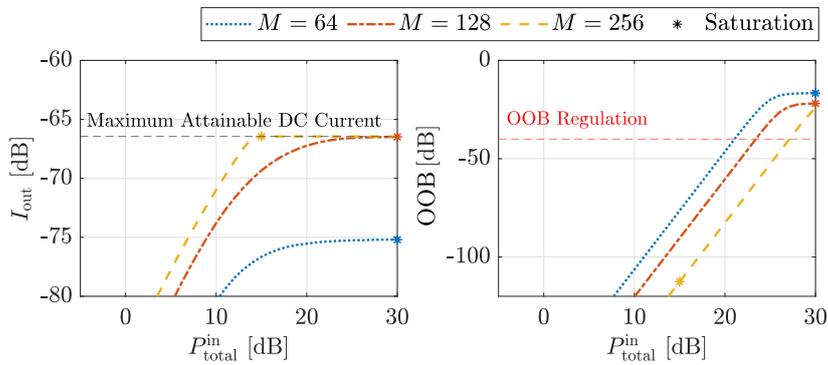
(a) Number of Used Tones, N, is equal to 2
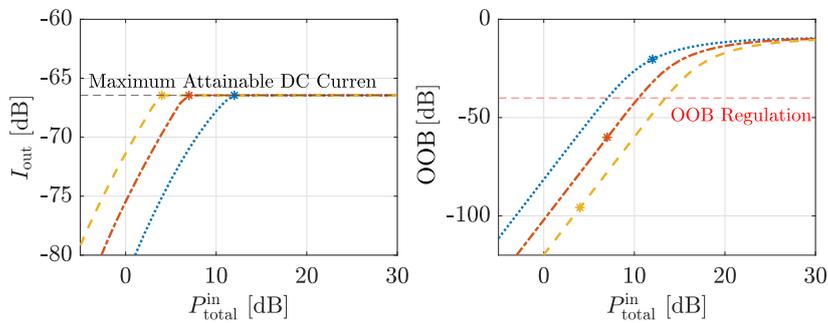
(b) Number of Used Tones, N, is equal to 20

Figure 4.8: i_out and OOB as a function of total input power for different number of antennas, Parameter configuration: $\beta = 3$, and the average correlated channel in Figure 4.1(b). Two cases, the number of tones, N, equals to 2 and 20, are shown.

$M = 256$ antennas and the number of tones equals 20. By leveraging the benefits of more antennas, we can effectively extend the coverage of the WPT system.
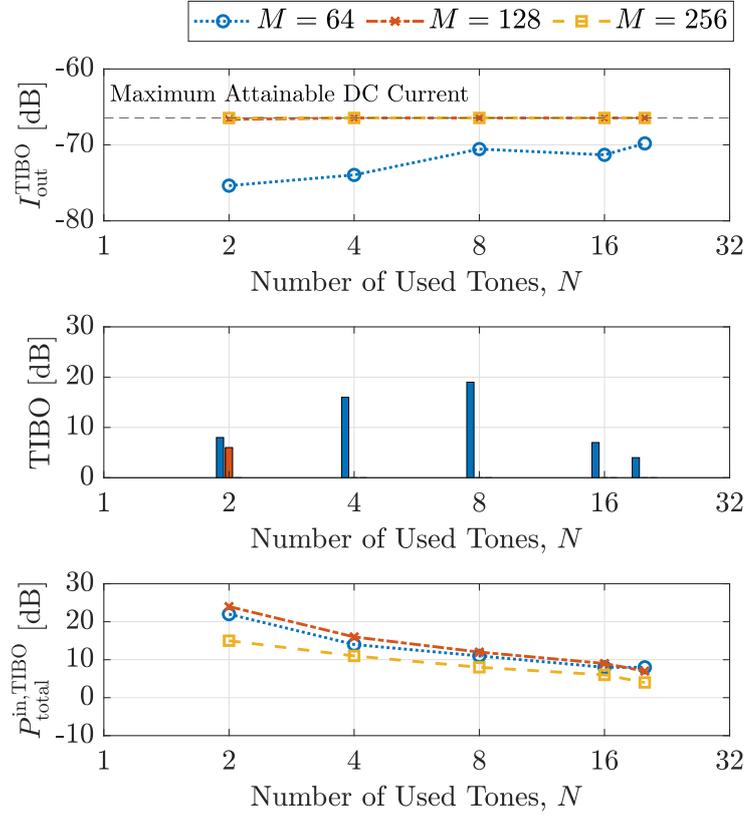
Figure 4.9: Attainable DC current considering the end-to-end effi-
ciency, $i_{\text{out}}^{\text{TIBO}}$ for the different number of antennas and tones.
TIBO and the corresponding input power level $P_{\text{total}}^{\text{in,TIBO}}$ is
shown together. Parameter configuration: $\beta = 3$, and the
average correlated channel in Figure 4.1(b).
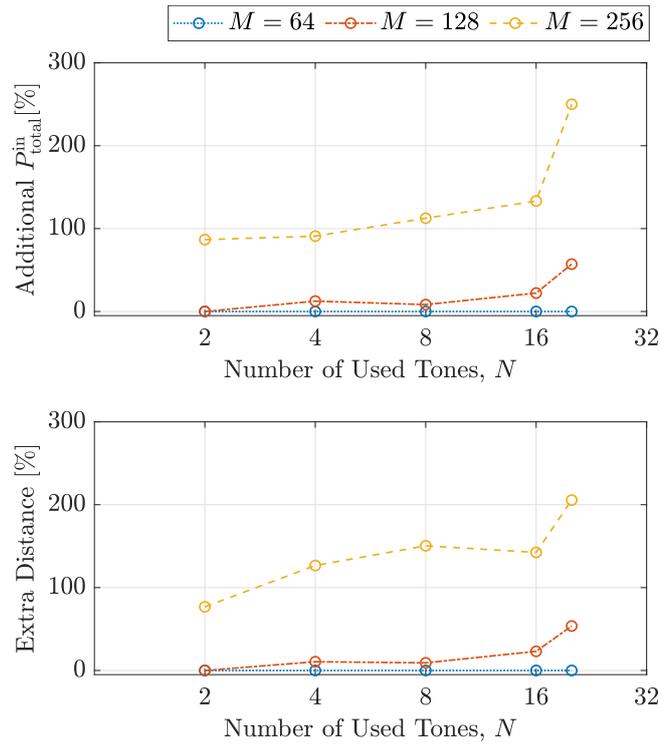
Figure 4.10: Additional $P_{\text{total}}^{\text{in}}$ and the extra distance that can be achieved for the number of antennas and tones based on free-space assumption. Parameter configuration: $\beta = 3$, and the average correlated channel in Figure 4.1(b). Note that in all of these curves except for $M = 64$, we achieve maximum output current at the ER and $\text{OOB} = -40$ dB.

4.3.3   Impact of Amplifier Characteristics

Now, we analyze the system performance varying the smoothing factor, β, in the SSPA model. The parameter β, indicates how "smooth" the transition is between the linear and non-linear behaviour of the PA. Figure 4.11 shows the actual responses of the SSPA with different values of β. As shown, when $\beta = 1$, the curve appears smoother than the other curves. This smoother response implies a greater distortion in the output signal, indicating a deviation from the desired amplification characteristics. Conversely, when β is increased to 3 and 5, the response moves closer to the ideal case.
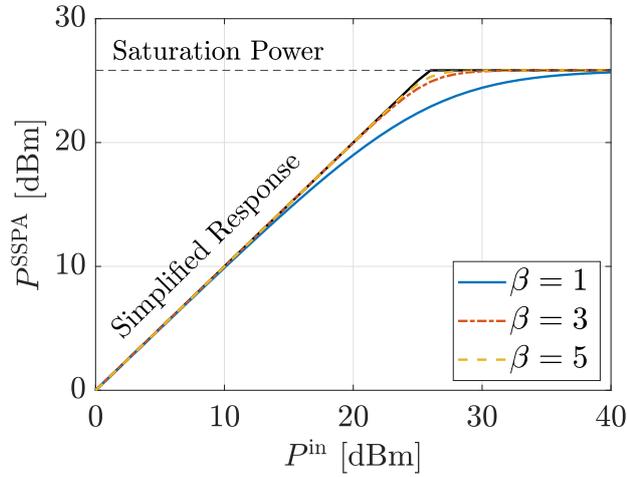
Figure 4.11: Actual SSPA responses where $G = 1$, $A_s = 0.875$ [V] for different β. Saturation power is calculated as $A_s^2/2$.

Roughly speaking, lower β values indicate poor amplifier quality. This study investigates the influence of the PA's quality on two key parameters: i_{out} and OOB. We analyze these parameters for the different number of tones, including values of 2, 4, 8, 16, and 20, while using $M = 128$ and considering the average correlated channel. Additionally, we analyze the impact on $i_{\text{out}}^{\text{TIBO}}$, along with the corresponding TIBO level. Furthermore, we explore the potential improvement in coverage when using different PA qualities, similar to the analysis conducted in the previous subsection.

Figure 4.12 shows the behaviour of i_{out} as a function of the total input power, $P_{\text{total}}^{\text{in}}$, along with the corresponding OOB, where β is equal to 1, 3, and 5. We consider two cases of the number of tones, where N is equal to 2 and 20. From the subfigures of Figure 4.12 (left), we observe that the i_{out} curves saturate faster as β increases. This indicates that for higher β values, the signals are less affected by PAs' distortion, resulting in higher transmitted power levels. This behaviour can be attributed to a higher β leading to a smoother transition between the linear and non-linear regions of the PA's response. We can also observe that OOB increases faster when β is low, as shown in the subfigures of Figure 4.12 (right), reflecting

higher distortion due to the poorer quality PAs, and we have found higher OOB requires more TIBO to retain the efficiency at the ET. Figure 4.13 presents an overview of the overall $i_{\text{out}}^{\text{TIBO}}$, the required TIBO level, and $P_{\text{total}}^{\text{in,TIBO}}$ for various number of tones and PA quality. As expected, the poor quality of the PAs with $\beta = 1$ requires more TIBO for any value of the number of antennas N, resulting in degraded $i_{\text{out}}^{\text{TIBO}}$ performance. On the other hand, we can observe that the performance of the two cases of β being equal to 3 and 5 shows similar trends on $i_{\text{out}}^{\text{TIBO}}$, while $\beta = 3$ has TIBO of 6 dB where the number of tones, N, is equal to 2.

(a) Number of Used Tones, N, is equal to 2

(b) Number of Used Tones, N, is equal to 20
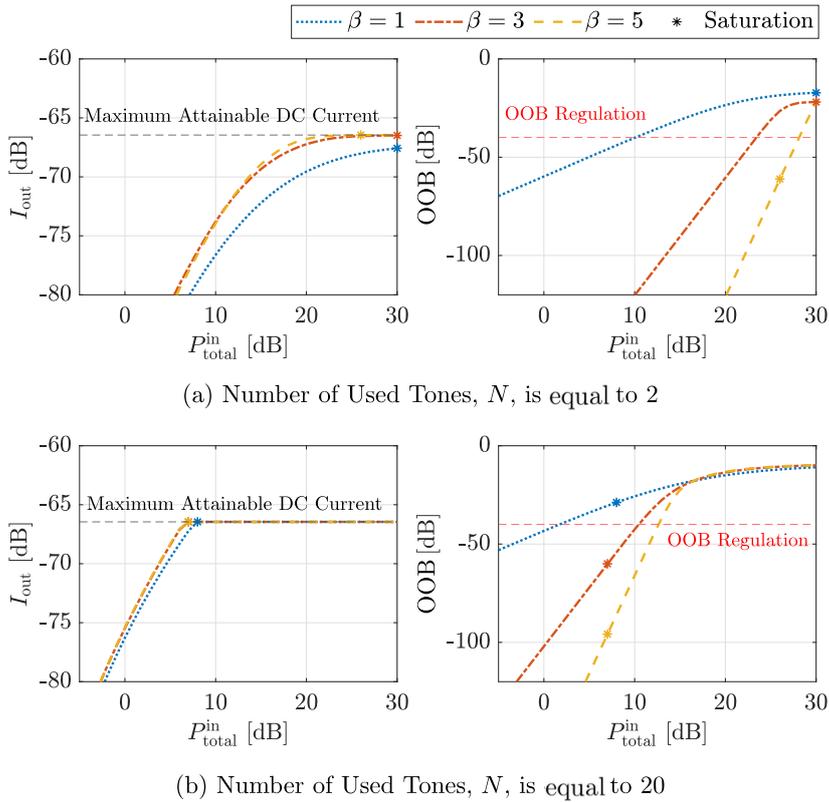
Figure 4.12: i_{out} and OOB as a function of total input power for the different values of β on SSPA. Parameter configuration: $M = 128$ and the average correlated channel in Figure 4.1(b). Two cases, with the number of tones, N, equals to 2 and 20, are shown.
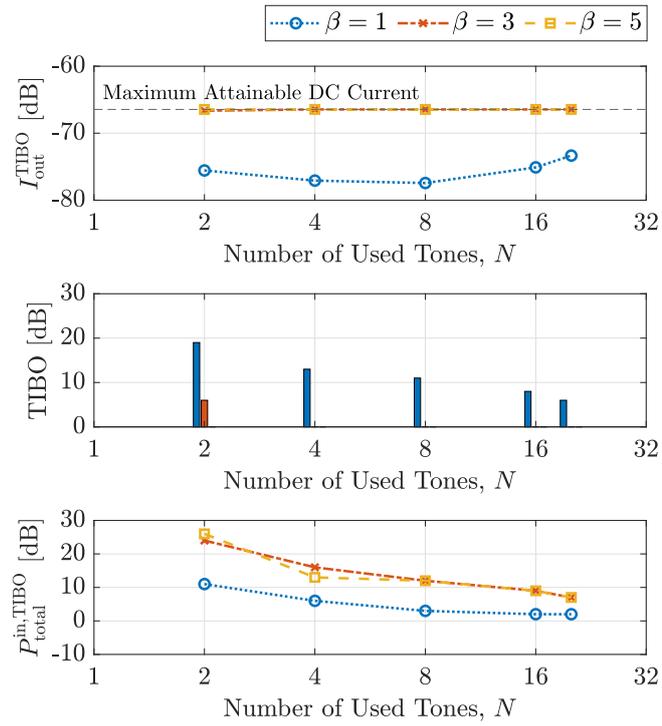
Figure 4.13: Attainable DC current considering the end-to-end efficiency, $i_{\text{out}}^{\text{TIBO}}$ for the different number of tones and β on SSPA. TIBO and the corresponding input power level $P_{\text{total}}^{\text{in,TIBO}}$ is shown together. Parameter configuration: $M = 128$ and the average correlated channel in Figure 4.1(b).

From the various OOB levels achieved by using different PA qualities, we can also analyze the influence of PA qualities on the additional distance the device can be charged from the ET. Figure 4.14 shows the additional $P_{\text{total}}^{\text{in}}$ we can obtain at most to adhere to the OOB regulation of -40 dB, along with the corresponding extra distance achievable, for the number of tones and PA qualities. We can observe that higher values of β, representing better quality PAs with reduced OOB, allow for greater additional distance to be achieved. This implies that the quality of the PAs impacts the system's capabilities, especially in terms of extending the charging range for devices.
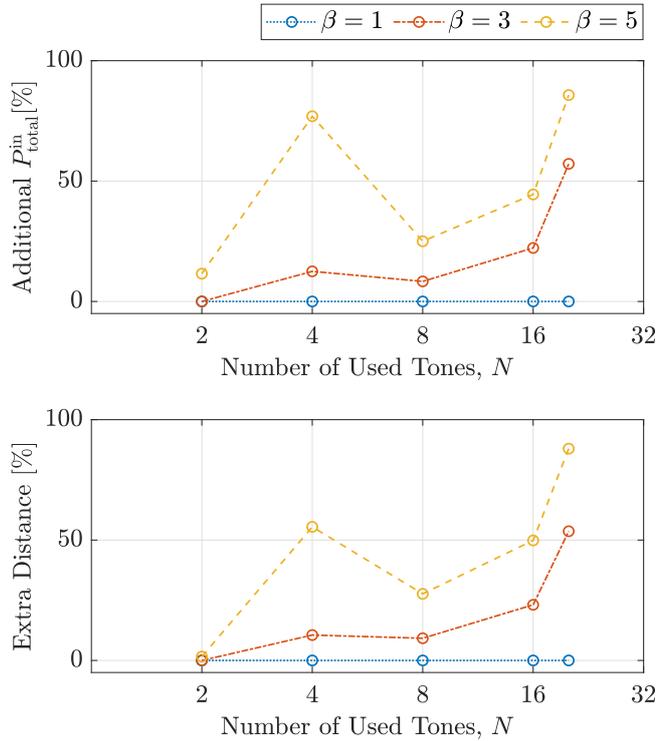
Figure 4.14: Additional $P_{\text{total}}^{\text{in}}$ and the extra distance that can be achieved for the different values of β on SSPAs and PA's qualities based on free-space assumption. Parameter configuration: $M = 128$ antenna, and the average correlated channel in Figure 4.1(b). Note that in all of these curves except for the $\beta = 1$, we achieve maximum output current at the ER and OOB $= -40$ dB.

4.3.4   Influence of Different Channel Correlations

Now we focus on analyzing and comparing the performance of the WPT system under different channel correlation scenarios. We aim to understand how channel correlation variations affect the system's performance by examining the five other channel models previously described. Specifically, we will investigate the impact of different channel correlations on the behaviours of i_{out}, OOB, TIBO level, attainable DC current $i_{\text{out}}^{\text{TIBO}}$ considering the end-to-end efficiency, and the corresponding input power, $P_{\text{total}}^{\text{in,TIBO}}$. For the other parameter configurations in this scenario, we used $M = 128$ and $\beta = 3$ on SSPA.

Figure 4.15 shows the i_{out} performance as a function of total input power along with the corresponding OOB in the five channel models. We consider the number of tones, N, to be equal to 2 and 20. Analyzing subfigures in Figure 4.18 (right), the rate of increase in OOB is notably higher for the free-space channel compared to the other Rayleigh channels. In contrast, Rayleigh fading channels exhibit remarkably similar trends in OOB. The higher OOB levels in the free-space channel are because, when implementing MRT on the LOS channel, the signal becomes more prone to distortion from the amplifiers at the ET. In the LOS channel, the MRT allocates uniform power across all available subcarriers, as there is no fading. All subcarriers experience the same channel gain and get a corresponding PAPR. On the other hand, in Rayleigh channels, the channel coefficients vary for antennas and subcarriers due to fading effects. When the channel coefficients are small for certain components, those components may not provide significant power allocation, and thus, MRT allocates less power to those components. This results in a reduced PAPR compared to the LOS case. We can further assess the high distortion experienced by the free-space channel in Figure 4.15 (b, left). The free-space case demands more input power to achieve the maximum attainable DC current. This circumstance arises from the reduced transmit power due to the distortion introduced by the amplifiers dealing with higher peak signals in the free-space channel.

Figure 4.16 presents an overall view of the attainable DC output current considering the end-to-end efficiency, $i_{\text{out}}^{\text{TIBO}}$, the required TIBO level, and corresponding $P_{\text{total}}^{\text{in,TIBO}}$ for different channel models and the number of tones, N, set to 2, 4, 8, 16, and 20. The figure shows that the free-space channel exhibits higher TIBO requirements than the other Rayleigh channels, as discussed earlier, due to its higher PAPR signals. This higher TIBO requirement decreases the performance of $i_{\text{out}}^{\text{TIBO}}$ for the free-space channel compared to the other Rayleigh channels.

Interestingly, by considering the end-to-end efficiency, the performance of WPT is better in Rayleigh channels than in a free-space channel. This comparison highlights the importance of considering channel characteristics in waveform design and power allocation strategies for end-to-end WPT systems. By leveraging fading and correlation attributes, the system can achieve better performance, making it more suitable for practical applications in real-world scenarios.

(a) Number of Used Tones, N, is equal to 2

(b) Number of Used Tones, N, is equal to 20
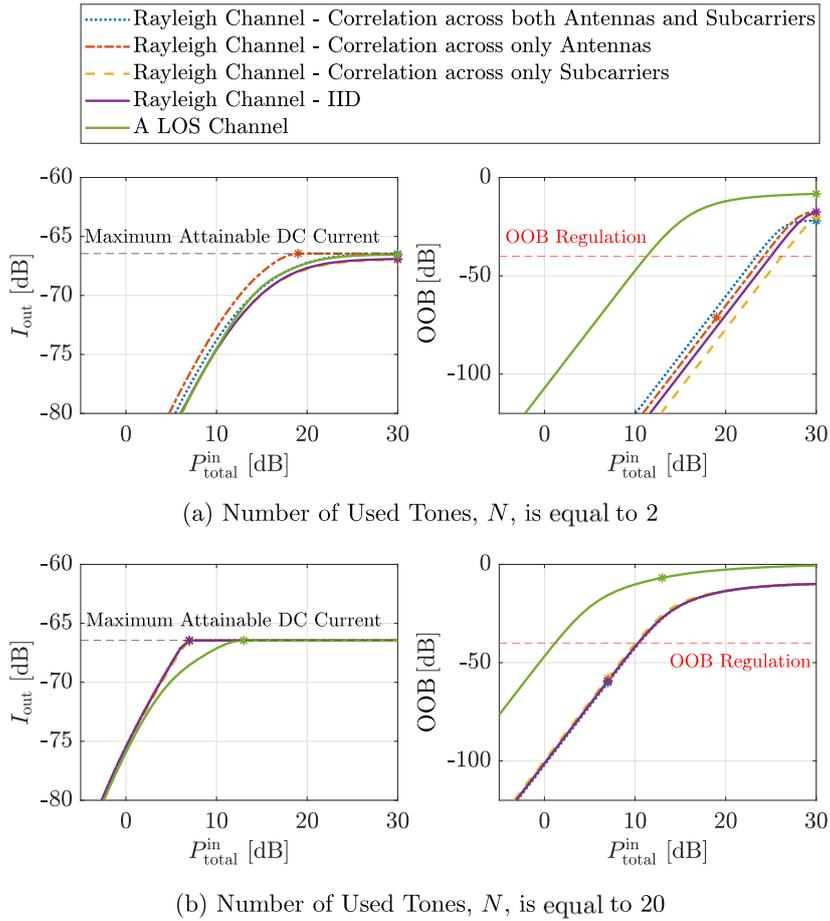
Figure 4.15: i_{out} and OOB as a function of total input power for different channel correlations. Parameter configuration: $M = 128$ and $\beta = 3$. Two cases, with the number of tones, N, equals to 2 and 20, are shown.
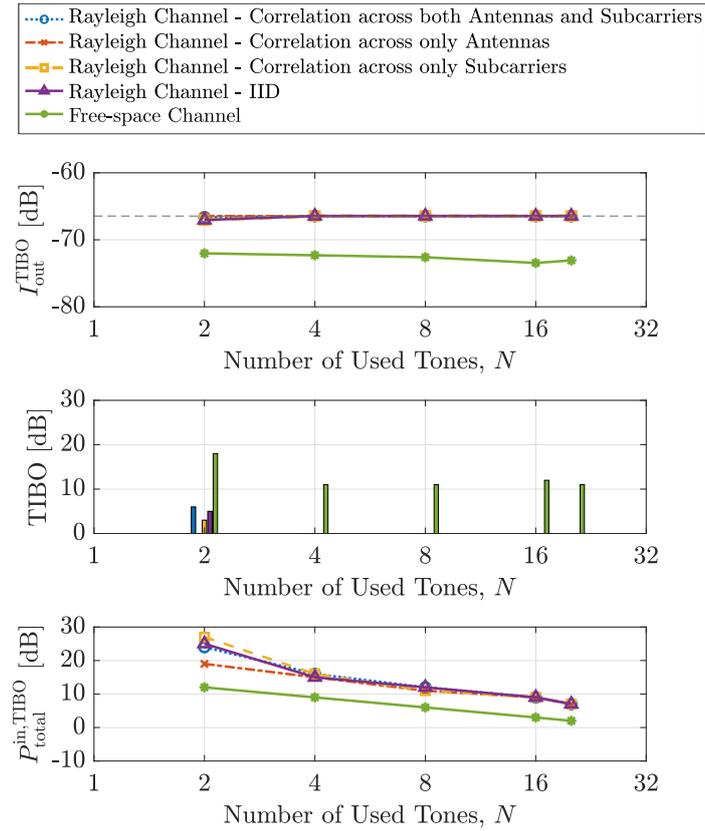
Figure 4.16: Attainable DC current considering the end-to-end efficiency, $i_{\mathrm{out}}^{\mathrm{TIBO}}$ for the different number of tones and channel correlations. TIBO and the corresponding input power level $P_{\mathrm{total}}^{\mathrm{in,TIBO}}$ is shown together. Parameter configuration: $M = 128$ and $\beta = 3$.

4.3.5   Tone Selection Schemes

In this subsection, we propose a tone selection scheme to enhance the end-to-end efficiency and show the performance of the proposed scheme in our system using MRT. The configurations considered are as follow: the number of tones, N, is equal to 2, 4, 8, 16, and 20, $M = 128$, $\beta = 3$, and the average correlated channel. We then compare the performance with the equally spaced tone selection scheme we used in our previous simulations as our default tone selection. To better understand the influence of different tone selection schemes, we include an additional tone selection scheme introduced in [17], where the strongest N subcarriers are selected, by computing norms across all antennas, out of all available subcarriers within the bandwidth, which is 1200 in our case.

   So far, the study has provided better understanding into the impact of a high peak signal on both PAs at the ET and rectifier at the ER. From the analysis, several aspects can be discussed:

   — **Impact on ET Efficiency**: An increase in the signal peak level consistently leads to a reduction in the efficiency of the ET. This is primarily attributed to the distortion introduced by the amplifiers.

   — **Impact on ER Efficiency:** For the ER, a higher peak signal proves to be beneficial for efficiency up to some $N^{\text{lim.}}$, beyond which the peaks become too short to charge the capacitor, where $N^{\text{lim.}} = 20$ in our system.

   — **Role of PAPR and Received Power:** Our simulation results indicate that increasing the PAPR can significantly enhance the ER, within the limitation of $N^{\text{lim.}}$, compared to solely focusing on improving received power levels.

Based on this understanding, we design a tone selection scheme in which each antenna selects the N strongest tones from a set of equally spaced $N^{\text{lim.}} = 20$ tones. This strategy provides several key aspects: *i)* By focusing on the selection of only N tones per antenna, we ensure the efficiency of the ET when operating with a smaller number of tones, N. *ii)* With a substantial number of antennas, $M = 128$, the chosen tones across all antennas are highly likely to contain the complete set of $N^{\text{lim.}} = 20$ tones, particularly within the context of the Rayleigh channel. *iii)* As the transmitted signals are received at the receiver in phase through MRT, the PAPR of the received signal corresponds to $N^{\text{lim.}} = 20$, maximizing the efficiency of ER in our setup. By adopting this approach, the proposed tone selection scheme is composed to enhance the efficiency at the ET, while leveraging the maximum efficiency at the ER. Figure 4.17 shows the addressed three tone selection schemes for the number of tones, N, set to 10, $M = 128$, and 1200 available subcarriers within the bandwidth. Figure 4.17(a) illustrates the selection of 10 tones, which are equally spaced 120 subcarriers apart. In Figure 4.17(b), the scheme selects the 10 strongest norms across the antennas out of the 1200 available subcarriers. In these two schemes, the PAPRs of signals on both the ET and ER are influenced by the 10 selected tones. On the other hand, Figure 4.17(c) illustrates the proposed tone selection scheme, selecting the 10 strongest tones out of the equally spaced $N^{\text{lim.}} = 20$ tones. In this figure, we observe that some antennas choose the same tones, while others choose different tones, resulting in a combination that covers

the complete set of $N^{\text{lim.}} = 20$ tones. From a PAPR perspective, this tone selection strategy maintains a consistent distortion level at the ET, where $N = 10$ tones are chosen. However, at the ER, we can receive a higher peak signal, where $N = 20$ tones are used.

(a) Equally spaced tone selection.

(b) N strongest norms selection.

(c) Proposed tone selection.
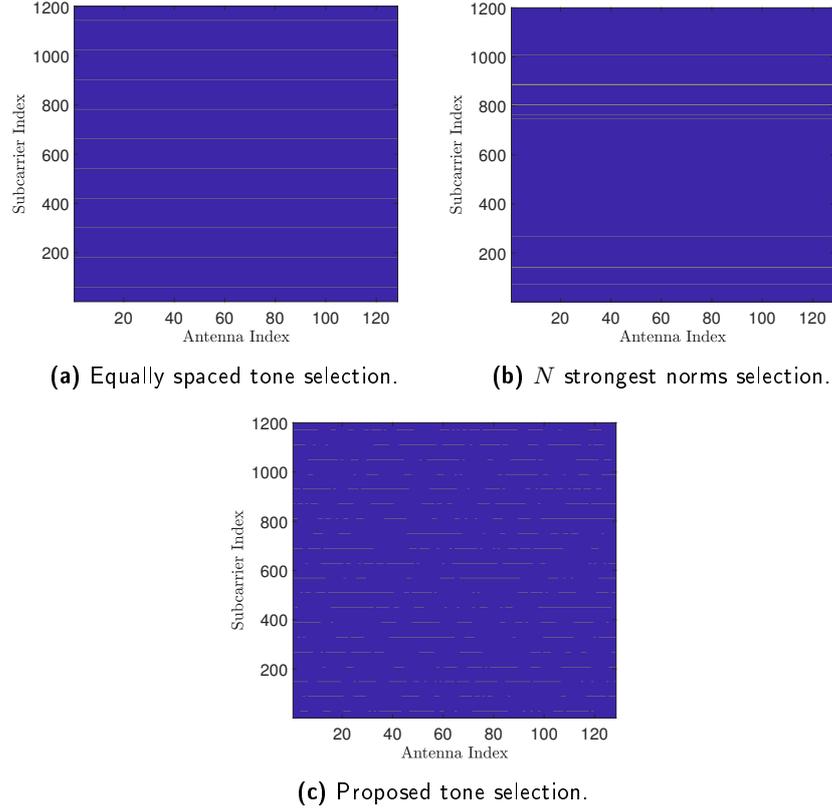
Figure 4.17: Different tone selection schemes. Yellow indicates indices of the selected tones.

Now, our focus shifts to evaluating the proposed tone selection scheme in our system, comparing it to two other tone selection schemes. We begin by analyzing the performance based on two key parameters: the DC output current, i_{out}, and OOB. These parameters are examined for different numbers of tones, specifically values of 2, 4, 8, 16, and 20, with $M = 128$, $\beta = 3$ for the SSPA, and considering the average correlated channel. Furthermore, we assess the $i_{\text{out}}^{\text{TIBO}}$ performance, which is attainable DC current considering the end-to-end efficiency, along with the corresponding TIBO level, in the different tone selection schemes.

Figure 4.18 displays the i_{out} performance as a function of the total input power, along with the corresponding OOB, for different tone selection schemes. Specifically, two cases are considered: $N = 2$ tones and $N = 20$ tones. Analyzing Figure 4.18(a), where $N = 2$ tones, the efficiency of the proposed tone selection

scheme becomes evident. The yellow dashed line in Figure 4.18(a, left) represents
the proposed scheme, requiring a total input power of 12 dB to reach saturation.
In contrast, the equally spaced tone selection requires 24 dB of total input power
considering TIBO, $P_{\text{total}}^{\text{in,TIBO}}$, and the strongest norms selection demands 16 dB.
Notably, the proposed scheme significantly reduces the input power requirement
for achieving the maximum DC current, highlighting its efficiency. Conversely,
when N is set to 20 in Figure 4.18(b), the proposed tone selection aligns with the
equally spaced tone selection, as N equals $N^{\text{lim.}}$, which is 20. In this case, the
strongest norms selection outperforms the others by utilizing stronger subchannels,
resulting in improved performance. Figure 4.19 highlights the effectiveness of the

(a) Number of Used Tones, N, is equal to 2

(b) Number of Used Tones, N, is equal to 20
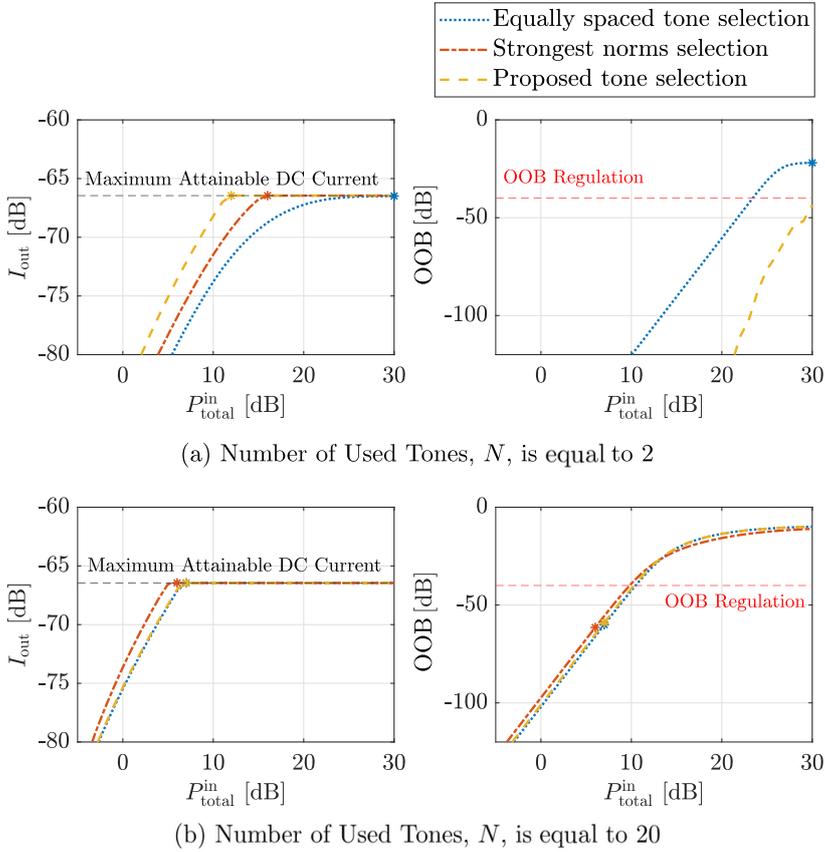
Figure 4.18: i_{out} and OOB as a function of total input power
for different tone selection schemes. Parameter configuration:
$M = 128$, $\beta = 3$, and average correlated channel. In two cases,
the number of tones, N, is equal to 2 and 20, are shown.

proposed tone selection scheme in achieving the attainable DC output current,
$i_{\text{out}}^{\text{TIBO}}$, along with the corresponding TIBO and $P_{\text{total}}^{\text{in,TIBO}}$ levels. The figure shows
the performance across different values of N. In cases where TIBO is not required,
which applies to all scenarios except for $N = 2$ in the equally spaced tone selection,

we focus on the $P_{\text{total}}^{\text{in,TIBO}}$ level. It is important to note that in these cases, $P_{\text{total}}^{\text{in,TIBO}}$ is equivalent to $P_{\text{total}}^{\text{in}}$, as no total input power backoff is needed. Analyzing the curves of $P_{\text{total}}^{\text{in,TIBO}}$, it is evident that the proposed tone selection scheme demands lower input power to reach the maximum attainable DC current, corresponding to the saturation point. This observation holds for scenarios where the number of tones, N, is less than $N^{\text{lim.}} = 20$.

The demonstrated effectiveness of the proposed tone selection scheme highlights its potential to offer more efficient transfer in practical scenarios, thereby contributing to the improvement of the end-to-end WPT performance.

Figure 4.19: Attainable DC current considering the end-to-end efficiency, $i_{\text{out}}^{\text{TIBO}}$ for the different number of tones, N, and tone selection schemes. TIBO and the corresponding input power level $P_{\text{total}}^{\text{in,TIBO}}$ is shown together. Parameter configuration: $M = 128$, $\beta = 3$, and average correlated channel.
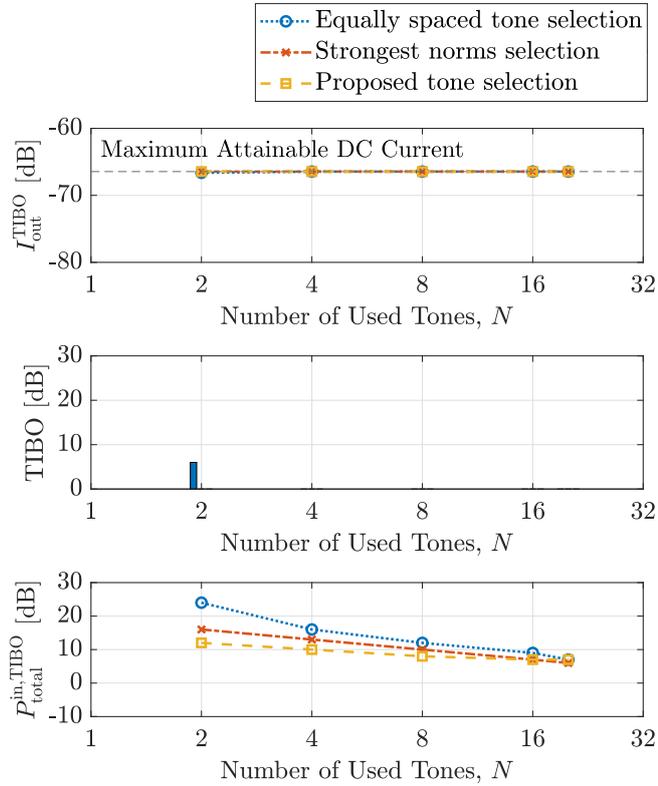
Conclusion and Future Work

5.1 Conclusion

In this thesis, we analyzed two waveform design schemes, focusing on their impact on DC output current at the ER, considering end-to-end WPT efficiency. We explored the SCP optimization and MRT scheme as two approaches to waveform design.

Initially, we investigated the SCP optimization approach, considering a constrained configuration with a limited number of tones and antennas due to the complexity of the SCP algorithm. Through this analysis, we studied the power allocation strategy of SCP, which is designed to optimize the DC current at the ER, considering the efficiency of the ET. We observed that the power allocation pattern in the SCP scheme exhibited similarities to the power allocation achieved through the MRT scheme. Both approaches allocate more power to strong sub-channels, leading to similar power distribution strategies.

Building upon this insight, we designed a WPT system based on the MRT scheme. We further investigated the factors influencing the DC output current at the ER, taking into account the efficiency of the ET under various scenarios, including variations in the number of tones, the number of antennas, amplifier quality, and different channel conditions. This system design enabled us to leverage a high number of antennas, up to 256, while significantly reducing the computational complexity compared to the SCP algorithm. As a result of this complexity reduction, we could extend the number of tones employed in the system to several thousand. However, our analysis revealed that as the number of tones, N, exceeded a certain threshold, the resulting signals became too short to effectively charge the harvester, leading to a rapid decline in efficiency at the ER. As a result, we found this threshold value as the maximum number of tones, $N^{\text{lim.}}$, and employed it as an upper limit.

Throughout our investigation, based on the MRT scheme, across diverse scenarios, we have several conclusions: *i)* Elevating the number of tones up to the maximum value of N amplified the efficiency of the ER, fostering accelerated growth in the harvested DC current. Nonetheless, this increase in the number of tones also introduced higher distortion levels in the ET, which can be mitigated using TIBO and consequently reducing the DC output current. *ii)* Leveraging more antennas contributed to array gain, proportional to $10 \cdot \log(M)$, increasing the re-

ceived power and the DC output current at the ER. As power distribution spreads across more antennas, the distortion level in power amplifiers is reduced. This reduction in distortion allowed for higher input power while maintaining a limit on distortion, thereby extending the coverage area for charging devices. Our setup with 256 antennas and 20 tones achieved a $+205\%$ increase in charging distance. *iii)* Amplifier quality plays a significant role in the system's performance. As expected, amplifiers of inferior quality, which operate more in non-linear regions, introduced higher distortion at the ET, leading to reduced DC output current. *iv)* Our analysis of different channel correlation scenarios highlighted that uniform power distribution across tones in a free-space channel, using all tones for generating a signal, introduced more distortion in power amplifiers compared to Rayleigh channels, which exploited the effective tones identified by MRT.

Based on our understanding, we introduced a tone selection scheme aimed at maximizing a PAPR of the received signal at the ER while maintaining the efficiency at the ET. Furthermore, we demonstrated our proposed scheme outperformed the other tone selection schemes: the equally spaced tone selection scheme and the scheme based on selecting the N strongest norms.

In summation, our thesis contributes an understanding of the complex interplay of the MRT waveform design scheme, various system parameters, channel characteristics, and tone selection scheme in WPT. By studying the intricacies of these factors, we offer guidance for designing and implementing efficient WPT systems across a range of practical scenarios. The demonstrated effectiveness of the proposed tone selection scheme highlights its potential to offer more efficient transfer in practical scenarios, thereby contributing to the improvement of the end-to-end WPT performance.

5.2 Future Work

With the purpose of advancing the practical applicability of our research, this subsection presents promising opportunities for future study. Specifically, we highlight the following directions that hold substantial potential for enriching our findings:

— **Increase the PAPR constraint at the harvester**: Expanding the scope of investigations to accommodate the higher PAPR constraints holds the potential for further enhancing the efficiency of the ER and the effectiveness of the proposed tone selection scheme. This expansion could involve examining various levels of device power consumption corresponding to different load resistances. Multiple diode rectifiers [13] can potentially increase the constraints. In our model, deriving the constraint in (2.24) assumes the use of a simple single-diode rectifier. Investigating the more advanced rectifier models could provide an additional increase in the PAPR constraint.

— **Multiple Users:** An fascinating opportunity for further research involves extending the study to encompass scenarios with multiple users. Investigating more dynamic waveform design strategies [14] in more complex setups could provide valuable insights into integrating the system into real-world applications.

References

[1] Zhengquan Zhang, Yue Xiao, Zheng Ma, Ming Xiao, Zhiguo Ding, Xianfu Lei, George K. Karagiannidis, and Pingzhi Fan. 6G wireless networks: Vision, requirements, architecture, and key technologies. *IEEE Vehicular Technology Magazine*, 14(3):28–41, 2019.

[2] Tongyi Huang, Wu Yang, Jun Wu, Jin Ma, Xiaofei Zhang, and Daoyin Zhang. A survey on green 6G network: Architecture and technologies. *IEEE Access*, 7:175758–175768, 2019.

[3] Ian F. Akyildiz, Ahan Kak, and Shuai Nie. 6G and beyond: The future of wireless communications systems. *IEEE Access*, 8:133995–134030, 2020.

[4] Harsh Tataria, Mansoor Shafi, Andreas F. Molisch, Mischa Dohler, Henrik Sjöland, and Fredrik Tufvesson. 6G wireless systems: Vision, requirements, challenges, insights, and opportunities. *Proceedings of the IEEE*, 109(7):1166–1199, 2021.

[5] Faiza Arshad, Jiao Lin, Nagesh Manurkar, Ersha Fan, Ali Ahmad, Maher un Nisa Tariq, Feng Wu, Renjie Chen, and Li Li. Life cycle assessment of lithium-ion batteries: A critical review. *Resources, Conservation and Recycling*, 180:106164, 2022.

[6] C.M. Costa, J.C. Barbosa, R. Gonçalves, H. Castro, F.J. Del Campo, and S. Lanceros-Méndez. Recycling and environmental issues of lithium-ion batteries: Advances, challenges and opportunities. *Energy Storage Materials*, 37:433–465, 2021.

[7] Mandeep Kaur and Rajni Aron. A systematic study of load balancing approaches in the fog computing environment. *The Journal of Supercomputing*, 77, 02 2021.

[8] Mike Hayes, Julie Donnelly, Giorgos Fagas, Raphael Salot, Guillaume Savelli, Peter Spies, Gerd vom Boegel, Mario Konijnenburg, Ben Breitung, Claudio Gerbaldi, Aldo Romani, Luca Gammaitoni, and Steve Beeby. Enables: European infrastructure powering the internet of things. In *Smart Systems Integration; 13th International Conference and Exhibition on Integration Issues of Miniaturized Systems*, pages 1–8, 2019.

[9] Onel L. A. López, Hirley Alves, Richard Demo Souza, Samuel Montejo-Sánchez, Evelio Martin Garcia Fernández, and Matti Latva-Aho. Massive wireless energy transfer: Enabling sustainable IoT toward 6G era. *IEEE Internet of Things Journal*, 8(11):8816–8835, 2021.

[10] Bruno Clerckx, Alessandra Costanzo, Apostolos Georgiadis, and Nuno Borges Carvalho. Toward 1G mobile power networks: RF, signal, and system designs to make smart objects autonomous. *IEEE Microwave Magazine*, 19(6):69–82, 2018.

[11] R. Want. An introduction to RFID technology. *IEEE Pervasive Computing*, 5(1):25–33, 2006.

[12] Nachiket Ayir, Taneli Riihonen, Markus Allén, and Marcelo Fabián Trujillo Fierro. Waveforms and end-to-end efficiency in RF wireless power transfer using digital radio transmitter. *IEEE Transactions on Microwave Theory and Techniques*, 69(3):1917–1931, 2021.

[13] Christopher R. Valenta and Gregory D. Durgin. Harvesting wireless power: Survey of energy-harvester conversion efficiency in far-field, wireless power transfer systems. *IEEE Microwave Magazine*, 15(4):108–120, 2014.

[14] Yong Zeng, Bruno Clerckx, and Rui Zhang. Communications and signals design for wireless power transmission. *IEEE Transactions on Communications*, 65(5):2264–2290, 2017.

[15] Bruno Clerckx and Ekaterina Bayguzina. Waveform design for wireless power transfer. *IEEE Transactions on Signal Processing*, 64(23):6313–6328, 2016.

[16] Yang Huang and Bruno Clerckx. Large-scale multiantenna multisine wireless power transfer. *IEEE Transactions on Signal Processing*, 65(21):5812–5827, 2017.

[17] Samith Abeywickrama, Rui Zhang, and Chau Yuen. Refined nonlinear rectenna modeling and optimal waveform design for multi-user multi-antenna wireless power transfer. *IEEE Journal of Selected Topics in Signal Processing*, 15(5):1198–1210, 2021.

[18] Yumeng Zhang and Bruno Clerckx. Waveform optimization for wireless power transfer with power amplifier and energy harvester non-linearities. In *ICASSP 2022 - 2022 IEEE International Conference on Acoustics, Speech and Signal Processing (ICASSP)*, pages 8632–8636, 2022.

[19] A. Collado and A. Georgiadis. Optimal waveforms for efficient wireless power transmission. *IEEE Microwave and Wireless Components Letters*, 24(5):354–356, 2014.

[20] C. RAPP. Effects of HPA-nonlinearity on a 4-DPSK/OFDM-signal for a digital sound broadcasting system. *Proc. 2nd European Conf. Satellite Communications, Oct. 1991*, pages 179–184, 1991.

[21] Matti1 Latva-aho and Kari Leppänen. Key drivers and research challenges for 6G ubiquitous wireless intelligence. In *Whitepaper from 6G summit, Finland*, 2019.

[22] Sha Hu, Fredrik Rusek, and Ove Edfors. Beyond massive MIMO: The potential of data transmission with large intelligent surfaces. *IEEE Transactions on Signal Processing*, 66(10):2746–2758, 2018.

[23] Nafiseh Mazloum and Ove Edfors. Initial analysis of dynamic panel activation for large intelligent surfaces. In *2021 IEEE Workshop on Signal Processing Systems (SiPS)*, pages 18–22, 2021.

[24] Xiwen Jiang, Mirsad Čirkić, Florian Kaltenberger, Erik G. Larsson, Luc Deneire, and Raymond Knopp. Mimo-tdd reciprocity under hardware imbalances: Experimental results. In *2015 IEEE International Conference on Communications (ICC)*, pages 4949–4953, 2015.

[25] Yong Zeng and Rui Zhang. Optimized training design for wireless energy transfer. *Communications, IEEE Transactions on*, 63:536–550, 02 2015.

[26] Jie Xu and Rui Zhang. Energy beamforming with one-bit feedback. *IEEE Transactions on Signal Processing*, 62(20):5370–5381, 2014.

[27] Jie Xu and Rui Zhang. A general design framework for mimo wireless energy transfer with limited feedback. *IEEE Transactions on Signal Processing*, 64(10):2475–2488, 2016.

SCP Theory

The optimization problem in (3.9) has a convex objective function which can be solved by SCP. In order to solve this problem using SCP, the objective function has to be linearly approximated by its first-order Taylor expansion at an operating point. This gives a new optimization problem where its solution is used to find the next operating point and so on. Doing this we obtain

$$z_{\text{DC}}^{(l)}(\overline{\mathbf{W}}^{\text{tr}}, \widehat{\mathbf{W}}^{\text{tr}}) = \sum_{m=1}^{M} \sum_{n=0}^{N-1} \bar{\alpha}_{n,m}^{(l)} \overline{W}_{n,m}^{\text{tr}^2} + \hat{\alpha}_{n,m}^{(l)} \widehat{W}_{n,m}^{\text{tr}^2}, \tag{A.1}$$

which gives the first-order Taylor expansion of the quantity z_{DC} at the lth iteration. Here, $\{\bar{\alpha}_{n,m}^{(l)}\}$ and $\{\hat{\alpha}_{n,m}^{(l)}\}$ represent the sequence of the first-order Taylor coefficients at the lth iteration which are computed by using the previous operating point $(\overline{\mathbf{W}}^{\text{tr}}, \widehat{\mathbf{W}}^{\text{tr}})^{(l-1)}$. Using this approximation, the optimization problem in (3.9) can now be written into

$$\max_{\overline{\mathbf{W}}^{\text{tr}}, \widehat{\mathbf{W}}^{\text{tr}}} \quad z_{\text{DC}}^{(l)}(\overline{\mathbf{W}}^{\text{tr}}, \widehat{\mathbf{W}}^{\text{tr}}) \tag{A.2}$$

$$\text{s.t.} \sum_{m=1}^{M} \frac{1}{2T} \int_{T} \left(\frac{x_m^{\text{tr}}(t)}{G} \cdot \left[\frac{1}{1 - \left(\frac{x_m^{\text{tr}}(t)}{A_s}\right)} \right]^{\frac{1}{2\beta}} \right)^2 dt \leqslant P_{\max}^{\text{in}},$$

$$\frac{1}{2} \sum_{m=1}^{M} \sum_{n=0}^{N-1} \overline{W}_{n,m}^{\text{tr}^2} + \widehat{W}_{n,m}^{\text{tr}^2} \leqslant P_{\max}^{\text{tr}}.$$

Now, Problem (A.2) can be solved by using Barrier's method. However, this requires the reformulation of Problem (A.2) such that we do not have non-linear constraints. This can be done by expressing the optimization problem as follows

$$\min_{\overline{\mathbf{W}}^{\text{tr}}, \widehat{\mathbf{W}}^{\text{tr}}} \quad -z_{\text{DC}}^{(l)}(\overline{\mathbf{W}}^{\text{tr}}, \widehat{\mathbf{W}}^{\text{tr}}) + \sum_{q=1}^{2} I(f_q(\overline{\mathbf{W}}^{\text{tr}}, \widehat{\mathbf{W}}^{\text{tr}})), \tag{A.3}$$

where $I(x)$ is a function that satisfies the following

$$I(x) = \begin{cases} 0 & \text{for } x \leqslant 0 \\ \infty & \text{for } x > 0 \end{cases} \tag{A.4}$$

and $f_1(\overline{\mathbf{W}}^{\text{tr}}, \widehat{\mathbf{W}}^{\text{tr}})$ and $f_2(\overline{\mathbf{W}}^{\text{tr}}, \widehat{\mathbf{W}}^{\text{tr}})$ are expressed as

$$f_1(\overline{\mathbf{W}}^{\text{tr}}, \widehat{\mathbf{W}}^{\text{tr}}) = \frac{1}{2} \sum_{m=1}^{M} \sum_{n=0}^{N-1} \overline{W}_{n,m}^{\text{tr}^2} + \widehat{W}_{n,m}^{\text{tr}^2} - P_{\max}^{\text{tr}}, \tag{A.5}$$

$$f_2(\overline{\mathbf{W}}^{\text{tr}}, \widehat{\mathbf{W}}^{\text{tr}}) = \sum_{m=1}^{M} \frac{1}{2T} \int_T \left(\frac{x_m^{\text{tr}}(t)}{G} \cdot [\frac{1}{1 - (\frac{x_m^{\text{tr}}(t)}{A_s})}]^{\frac{1}{2\beta}} \right)^2 dt - P_{\max}^{\text{in}}. \tag{A.6}$$

In order to make the objective function in (A.3) differentiable, the function $I(x)$ can be approximated using the relationship

$$\hat{I}(x) = -\frac{1}{t} \log(-x) \tag{A.7}$$

where t is a parameter that determines how close $\hat{I}(x)$ gets to $I(x)$.

Now, we have an optimization problem where the objective function is differentiable and the constraints are linear.

$$\min_{\overline{\mathbf{W}}^{\text{tr}}, \widehat{\mathbf{W}}^{\text{tr}}} \quad -z_{\text{DC}}^{(l)}(\overline{\mathbf{W}}^{\text{tr}}, \widehat{\mathbf{W}}^{\text{tr}}) - \frac{1}{t} \sum_{q=1}^{2} \log(-f_q(\overline{\mathbf{W}}^{\text{tr}}, \widehat{\mathbf{W}}^{\text{tr}})). \tag{A.8}$$

To conclude, the optimization problem presented in (3.9) is solved iteratively using SCP where in each SCP iteration the optimization problem is approximated to (A.2). Problem (A.2) is then solved using Barrier's method which uses Newton's method.

The entire optimization problem is described in Algorithm 1 which uses Algorithm 2 which in itself uses Algorithm 3. In Algorithm 3 we used F to denote the expression in (A.3). It is important to note that in the below Algorithms 1-3, vector notations are used. Furthermore, when it comes to the SCP approach, the choice of parameters for the optimization algorithm plays a crucial role in determining the stability and convergence to optimal weights. Table A.1 lists the parameter set of SCP used in our simulation.

Algorithm 1: Successive convex programming

Input: $(\overline{\mathbf{W}}^{\mathrm{tr}}, \widehat{\mathbf{W}}^{\mathrm{tr}})^{(0)}$, $\epsilon_0 > 0$, $l \leftarrow 1$;
Output: $(\overline{\mathbf{W}}^{\mathrm{tr}}, \widehat{\mathbf{W}}^{\mathrm{tr}})^{\star}$;
Repeat:
  1: Compute $(\bar{\mathbf{a}}, \hat{\mathbf{a}})^{(l)}$ at the operating point $(\overline{\mathbf{W}}^{\mathrm{tr}}, \widehat{\mathbf{W}}^{\mathrm{tr}})^{(l-1)}$
     using Taylor expansion;
  2: Compute $(\overline{\mathbf{W}}^{\mathrm{tr}}, \widehat{\mathbf{W}}^{\mathrm{tr}})^{(l)}$ using Algorithm 2;
  3: Update $(\overline{\mathbf{W}}^{\mathrm{tr}}, \widehat{\mathbf{W}}^{\mathrm{tr}})^{\star} \leftarrow (\overline{\mathbf{W}}^{\mathrm{tr}}, \widehat{\mathbf{W}}^{\mathrm{tr}})^{(l)}$;
  4: Quit if $||\overline{\mathbf{W}}^{\mathrm{tr},(l)} - \overline{\mathbf{W}}^{\mathrm{tr},(l-1)}|| < \epsilon_0$;
  5: $l \leftarrow l + 1$

Algorithm 2: Barrier's method

Input: $(\overline{\mathbf{W}}^{\mathrm{tr}}, \widehat{\mathbf{W}}^{\mathrm{tr}})^{(B_0)}$, $t > 0$, $\mu_B > 0$, $\epsilon_B > 0$;
Output: $(\overline{\mathbf{W}}^{\mathrm{tr}}, \widehat{\mathbf{W}}^{\mathrm{tr}})^{(l)}$;
Repeat:
  1: Compute $(\overline{\mathbf{W}}^{\mathrm{tr}}, \widehat{\mathbf{W}}^{\mathrm{tr}})$ by minimizing Problem (A.8)
     using Newton's Method with initialized point $(\overline{\mathbf{W}}^{\mathrm{tr}}, \widehat{\mathbf{W}}^{\mathrm{tr}})^{(B_0)}$
  2: Update $(\overline{\mathbf{W}}^{\mathrm{tr}}, \widehat{\mathbf{W}}^{\mathrm{tr}})^{(l)} \leftarrow (\bar{\mathbf{w}}^{\mathrm{tr}}, \hat{\mathbf{w}}^{\mathrm{tr}})$;
  3: Quit if $2/t < \epsilon_B$;
  4: $t \leftarrow \mu_B t$, $(\overline{\mathbf{W}}^{\mathrm{tr}}, \widehat{\mathbf{W}}^{\mathrm{tr}})^{(B_0)} \leftarrow (\overline{\mathbf{W}}^{\mathrm{tr}}, \widehat{\mathbf{W}}^{\mathrm{tr}})^{(l)}$

Algorithm 3: Newton's method for optimization

Input: $(\overline{\mathbf{W}}^{\mathrm{tr}}, \widehat{\mathbf{W}}^{\mathrm{tr}})^{(k)} \leftarrow (\overline{\mathbf{W}}^{\mathrm{tr}}, \widehat{\mathbf{W}}^{\mathrm{tr}})^{(B_0)}$, $k \leftarrow 1$, $\gamma > 0$, $\epsilon_n > 0$
Output: $(\overline{\mathbf{W}}^{\mathrm{tr}}, \widehat{\mathbf{W}}^{\mathrm{tr}})$
Repeat:
  1: Compute the gradient ∇F and hessian $\nabla^2 F$ for Problem (A.8)
     at the point $(\overline{\mathbf{W}}^{\mathrm{tr}}, \widehat{\mathbf{W}}^{\mathrm{tr}})^{(k)}$
  2: Take the next step:
     $(\overline{\mathbf{W}}^{\mathrm{tr}}, \widehat{\mathbf{W}}^{\mathrm{tr}})^{(k+1)} = (\overline{\mathbf{W}}^{\mathrm{tr}}, \widehat{\mathbf{W}}^{\mathrm{tr}})^{(k)} - \gamma [\nabla^2 F]^{-1} \nabla F$
  3: Update $(\overline{\mathbf{W}}^{\mathrm{tr}}, \widehat{\mathbf{W}}^{\mathrm{tr}}) \leftarrow (\overline{\mathbf{W}}^{\mathrm{tr}}, \widehat{\mathbf{W}}^{\mathrm{tr}})^{(k+1)}$;
  4: Quit if $||\overline{\mathbf{W}}^{\mathrm{tr},(k+1)} - \overline{\mathbf{W}}^{\mathrm{tr},(k)}|| < \epsilon_n$;
  5: $(\overline{\mathbf{W}}^{\mathrm{tr}}, \widehat{\mathbf{W}}^{\mathrm{tr}})^{(k)} \leftarrow (\overline{\mathbf{W}}^{\mathrm{tr}}, \widehat{\mathbf{W}}^{\mathrm{tr}})^{(k+1)}$;
  6: $k \leftarrow k + 1$

Parameter Variable	Value
ϵ_0	$1 \cdot 10^{-3}$
t	$1 \cdot 10^{7}$
μ_B	1.2
ϵ_B	$5 \cdot 10^{-8}$
γ	$5 \cdot 10^{-5}$
ϵ_n	$1 \cdot 10^{-4}$

Table A.1: SCP optimization algorithm parameters